Please use this PDF proof to check the layout of your article. If you would like any changes to be made to the layout, you can leave instructions in the online proofing interface. First, return to the online proofing interface by clicking "Edit" at the top page, then insert a Comment in the relevant location. Making your changes directly in the online proofing interface is the quickest, easiest way to correct and submit your proof.

Please note that changes made to the article in the online proofing interface will be added to the article before publication, but are not reflected in this PDF proof.

Cell

Adult neural stem cell activation in mice is regulated by the day/night cycle and intracellular calcium dynamics

Graphical Abstract

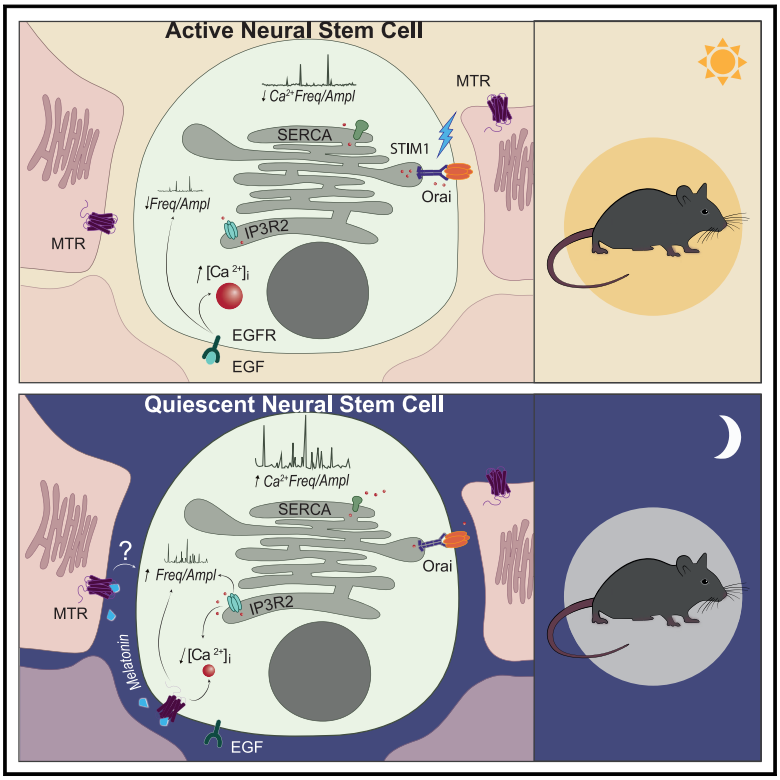

Highlights

- Adult neural stem cell (NSC) activation is regulated by the day/night cycle
- NSC states differ in Ca^{2+} dynamics and steady-state levels
- Darkness-induced melatonin signaling modulates NSC states via calcium
- Mimicking quiescent-state Ca^{2+} entry reverses switch to NSC proliferative state

Authors

Archana Gengatharan, Sarah Malvaut, Alina Marymonchyk, ..., Jovica Ninkovic, Magdalena Götz, Armen Saghatelyan

Correspondence

armen.saghatelyan@fmed.ulaval.ca

In Brief

Darkness-induced melatonin signaling modulates the proliferative state of neural stem cells through the modulation of Ca^{2+} dynamics as evidenced by live imaging and optogenetically induced "quiescent-state"-like calcium patterns in freely behaving mice.

Gengatharan et al., 2021, Cell *184*, 1–14
February 4, 2021
https://doi.org/10.1016/j.cell.2020.12.026

Please cite this article in press as: Gengatharan et al., Adult neural stem cell activation in mice is regulated by the day/night cycle and intracellular calcium dynamics, Cell (2021), https://doi.org/10.1016/j.cell.2020.12.026

Cell

CellPress

Article

Adult neural stem cell activation in mice is regulated by the day/night cycle and intracellular calcium dynamics

Archana Gengatharan,[1,2] Sarah Malvaut,[1,2] Alina Marymonchyk,[1,2] Majid Ghareghani,[1,2] Marina Snapyan,[1,2] Judith Fischer-Sternjak,[3,4] Jovica Ninkovic,[4,5] Magdalena Götz,[3,4,6] and Armen Saghatelyan[1,2,7,*]

[1]CERVO Brain Research Center, Quebec City, QC G1J 2G3, Canada
[2]Université Laval, Quebec City, QC G1V 0A6, Canada
[3]Division of Physiological Genomics, BioMedical Center, Ludwig-Maximilians-Universität München, Munich, Germany
[4]Institute of Stem Cell Research, Helmholtz Center, Munich, Germany
[5]Department of Cell Biology and Anatomy, Ludwig-Maximilians-Universität München, Munich, Germany
[6]Munich Cluster for Systems Neurology (SyNergy), Munich, Germany
[7]Lead contact
*Correspondence: armen.saghatelyan@fmed.ulaval.ca
https://doi.org/10.1016/j.cell.2020.12.026

SUMMARY

Neural stem cells (NSCs) in the adult brain transit from the quiescent state to proliferation to produce new neurons. The mechanisms regulating this transition in freely behaving animals are, however, poorly understood. We customized *in vivo* imaging protocols to follow NSCs for several days up to months, observing their activation kinetics in freely behaving mice. Strikingly, NSC division is more frequent during daylight and is inhibited by darkness-induced melatonin signaling. The inhibition of melatonin receptors affected intracellular Ca^{2+} dynamics and promoted NSC activation. We further discovered a Ca^{2+} signature of quiescent versus activated NSCs and showed that several microenvironmental signals converge on intracellular Ca^{2+} pathways to regulate NSC quiescence and activation. *In vivo* NSC-specific optogenetic modulation of Ca^{2+} fluxes to mimic quiescent-state-like Ca^{2+} dynamics in freely behaving mice blocked NSC activation and maintained their quiescence, pointing to the regulatory mechanisms mediating NSC activation in freely behaving animals.

INTRODUCTION

The adult mammalian brain has a remarkable capacity to produce new neurons that integrate into preexisting neuronal networks and that play a functional role in animal behavior (Akers et al., 2014; Anacker and Hen, 2017; Malvaut and Saghatelyan, 2016). These neurons are derived from adult neural stem cells (NSCs), and several studies have demonstrated that the generation and survival of new neurons are regulated by a diverse set of physiological stimuli and behavioral states, including physical exercise, stress, novel environments, diet, and social and maternal interactions (Obernier and Alvarez-Buylla, 2019; Paul et al., 2017; Urbán et al., 2019). It is, however, not known how the physiology of NSCs is influenced by different behavioral states in freely behaving mice that naturally explore their environment and undergo distinct behavioral-state-dependent changes. Live imaging of adult NSCs in zebrafish (Barbosa et al., 2015) and the murine dentate gyrus (Pilz et al., 2018) has provided profound new insights into their mode of division and their progeny. However, NSCs have so far only been examined in animals under anesthesia, which resembles a non-active, sleep-like state (Brown et al., 2010; Lewis et al., 2018) that affects the physiology of neurons and glia (Hemmings et al., 2005; Kim et al., 2018). We also know very little about the influence of the day/night cycle on NSC activity *in vivo*.

We thus developed a minimally invasive advanced technology that makes it possible to image NSCs in freely behaving mice for up to 2 months. Since the subventricular zone (SVZ) bordering the lateral ventricle contains the largest population of NSCs in the adult brain (Obernier and Alvarez-Buylla, 2019), we installed mini-endoscopes in the lateral ventricle to perform side-view imaging of NSCs in the intact SVZ. We also used two-color mini-endoscopic imaging allowing to monitor NSCs identified by the activity of the GFAP and prominin promoters (Beckervordersandforth et al., 2010; Codega et al., 2014). Our *in vivo* imaging approaches revealed that the dynamics of NSC activation are regulated by day/night cycle, with a higher propensity for division during the day. This regulation was dependent on day/night changes in melatonin levels. Altering melatonin signaling either pharmacologically or by keeping the mice in constant light or constant darkness for 3 or 7 days modified the number of proliferative NSCs.

Please cite this article in press as: Gengatharan et al., Adult neural stem cell activation in mice is regulated by the day/night cycle and intracellular calcium dynamics, Cell (2021), https://doi.org/10.1016/j.cell.2020.12.026

We then explored Ca^{2+} dynamics in NSCs as a possible mechanism for integrating and decoding the multiple signals impinging on NSCs. This revealed striking differences in the dynamics and steady-state intracellular levels of Ca^{2+} between the quiescent and proliferative states of NSCs and showed that several microenvironmental signals converge on intracellular Ca^{2+} to regulate NSC activation and the transition from the quiescent to the proliferative state. Importantly, blocking melatonin receptors also affected these characteristic differences, and *in vivo* optogenetic manipulation of Ca^{2+} fluxes into NSCs to mimic the Ca^{2+} dynamics of the quiescent state blocked the transition of NSCs to the proliferative state. NSC division in freely behaving mice is thus regulated by the day/night cycle and is dependent on intracellular Ca^{2+} dynamics, a key integrator of signals that regulate NSC activation versus quiescence.

RESULTS

Imaging SVZ NSC activation kinetics in freely behaving mice

To label adult NSCs *in vivo* and then follow their dynamics by live imaging, we electroporated CMV-GFP plasmids into the SVZ of postnatal day (P)0 to P1 CD1 pups (or CMV-RFP plasmids into GFAP-GFP pups) and analyzed label-retaining cells in adulthood (Figure 1A). As the plasmids were diluted by multiple rounds of division, only nondividing or slowly dividing cells retained the label (Figure 1B). Of the cells that retained XFP, 28.5% were nondividing Ki67-niche astrocytes that co-expressed GFAP and s100β, the latter being expressed by niche astrocytes, but not NSCs (Codega et al., 2014), while the majority (53.4% ± 2.5%) were slowly dividing NSCs ($GFAP^+/s100\beta^-$) (Figures 1C and 1D). Among the electroporated NSCs, 7.1% ± 1.7% were $Ki67^+$ and hence proliferating activated NSCs (aNSCs). To ensure labeling specificity, we took advantage of the previously established fact that NSCs, unlike astrocytes and ependymal cells, exhibit coincident activity of the GFAP and prominin (P2) promoters (Beckervordersandforth et al., 2010; Codega et al., 2014). When P0–P1 pups were electroporated with two plasmids that drive the expression of GFP and mCherry under the GFAP and P2 promoters, respectively, hardly any niche astrocytes were labeled, as almost all labeled cells were $s100\beta^-$. The percentage of activated $Ki67^+$ NSCs among $GFP^+/mCherry^+$ electroporated cells in the SVZ was 7.7% ± 1.0% at P60 (Figure 1E; Table S1), a virtually identical value to the one obtained by analyzing $GFAP^+/s100\beta^-/Ki67^+$ XFP cells described above. We could thus reliably label NSCs, a small proportion of which are activated at a given stage, which is consistent with previous work (Codega et al., 2014; Dulken et al., 2017; Leeman et al., 2018; Llorens-Bobadilla et al., 2015).

This labeling method enabled us to explore the dynamics of NSC division in freely behaving mice by live *in vivo* imaging. To achieve this, we used miniature microscopes (mini-endoscopes) connected to a gradient index (GRIN) lens (0.5 mm in diameter) inserted into the SVZ of adult mice (P60–P90) after electroporating CMV-GFP into P0–P1 pups (Figure 1F; Video S1**)**. Immunolabeling for Ki67 in the SVZ following the insertion of the GRIN lens did not reveal any changes in the number of proliferating NSCs (Figure S1). To further ascertain that the dynamics of NSC activation are not affected by the insertion of the GRIN lens into the SVZ, we also used a side-view mini-endoscope composed of a GRIN lens with a 45° prism glued to it (Figures 1F and 1G and S1). This mini-endoscope made it possible to perform side-view imaging of NSCs located at the lateral wall of the SVZ with the GRIN lens installed in the lateral ventricle (Figure 1G). No differences in the dynamics of NSC division were observed using either of these two mini-endoscopic implants. We could thus pool data from both approaches to image sparse label-retaining NSCs *in vivo*. Live imaging of adult NSCs (one image every 15 min) for several hours showed that a long quiescent phase is followed by a cell-division phase lasting 83.3 ± 11.4 min (n = 20 cells; Figures 1H and 1J; Table S1; Video S2). NSC division was defined as completed mitosis of the mother cell with high fluorescence intensity into two clearly discernable daughter cells with reduced fluorescence intensities due to the dilution of the fluorophore in the two daughter cells (Figure 1H; Videos S2 and S3). The start of cell division was defined as the first time frame preceding the reduction in fluorescence intensity (Figure 1H, 9:00 a.m.) and the end of cell division as the time frame when two clearly discernable cells are observed (Figure 1H, 9:30 a.m.). This analysis focused on cell division (i.e., the M phase) and did not measure the full cell-cycle length, including the typically long G1 phase. To ascertain the identity of the NSCs during the *in vivo* imaging, we also used a two-color mini-endoscope to image NSCs labeled by the co-electroporation of the CMV-RFP and P2-GFP plasmids and observed the same dynamics of NSC division (92.1 ± 20.3 min, n = 7 cells; Figures 1I and 1J; Table S1). Two-color imaging allowed NSC division to be detected in two different channels using two different promoter-driven fluorophores, which alleviated issues associated with cell movement that may arise during one-color imaging. This validated the robustness and sensitivity of mini-endoscopic imaging for monitoring NSC division in freely behaving mice. In all of these experiments, the NSCs remained in the same position and did not migrate during the imaging, which is consistent with a previous report showing that $GFAP\text{-}GFP^+$ and $nestin\text{-}GFP^+$ cells in the SVZ are static and nonmigratory in acute brain slice preparations (Kim et al., 2009).

Regulation of NSC activation by melatonin signaling

Our mini-endoscopic imaging in freely behaving mice made it possible to determine whether NSC division is regulated by different behavioral states and whether it is different during the day and the night. To this end, we continuously imaged NSCs for 2–3 days, with one acquisition every 15 min (Figure 2A; Video S4). Surprisingly, we observed a higher propensity for NSC division during the day compared to the night (Figure 2B). Approximately 70% of NSC division occurred during the day, with a peak at 2–5 h Zeitgeber time (ZT), corresponding to 9–12 a.m. (Figure 2B). To ascertain day/night differences in the activation of NSCs, we examined the number of $GFP^+/mCherry^+/Ki67^+$ cells in the fixed tissue, in the adult mice that had been electroporated at P0–P1 with the GFAP-GFP and P2-mCherry plasmids at ZT 8 (3 p.m.) and ZT 18 (1 a.m.). A higher proportion of proliferating NSCs was detected at ZT 8 (during the day) than at ZT 18 (during the night), which was consistent with the live imaging data (Figures 2C and 2D). This effect was specific to SVZ NSCs, as no

Please cite this article in press as: Gengatharan et al., Adult neural stem cell activation in mice is regulated by the day/night cycle and intracellular calcium dynamics, Cell (2021), https://doi.org/10.1016/j.cell.2020.12.026

CellPress

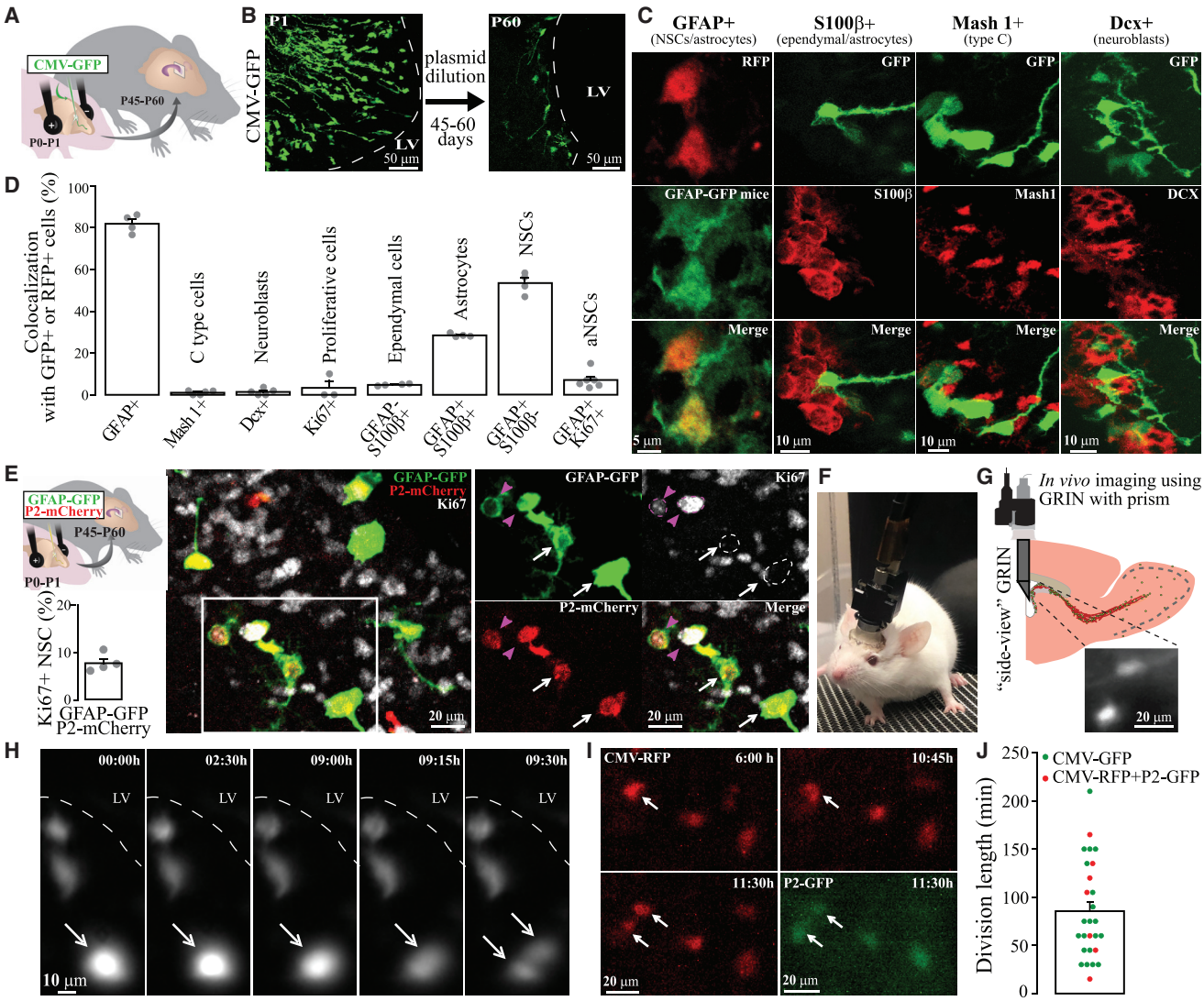

Figure 1. Imaging NSC division in freely behaving mice

(A and B) Schematic of the electroporation approach and the dilution of the plasmid from P1 to P60.

(C and D) Immunolabeling for cell-type-specific markers and quantification of label-retaining cells in the adult SVZ.

(E) Co-electroporation of GFAP-GFP and P2-mCherry to specifically label NSCs and quantify aNSCs. The white arrows indicate Ki67$^-$ NSCs, while the magenta arrowheads indicate Ki67$^+$ NSCs. The positions of qNSCs and aNSCs are shown by magenta and white regions of interest (ROIs), respectively, on the Ki67 image.

(F and G) Photomicrograph showing a mouse with a two-color mini-endoscope and a schematic drawing showing the location of the side-view GRIN lens.

(H and I) One-color and two-color mini-endoscopic imaging of NSCs in freely behaving mice. Arrows indicate dividing NSCs. Note the reduced fluorescence intensity in the daughter cells, which is consistent with the dilution of the plasmid.

(J) Quantification of division time.

Data are expressed as means ± SEM. The individual values of experiments (circles) are also shown. n = 4–6 mice for (D) and (E) and 27 cells from 13 mice for (J). For the experiments shown in (D) and (E), the mice were perfused at 1–3 p.m. See also Figure S1, Table S1, and Videos S1, S2, and S3.

difference in the density of niche astrocytes was observed (Figure S2). To further probe the influence of the day/night cycle on the regulation of NSC division, we kept adult GFAP-GFP and P2-mCherry electroporated mice for 3 or 7 days in complete darkness. The control mice were kept on a 12-h/12-h light/dark cycle (Figure 2E). Immunolabeling for Ki67 revealed no difference with 3 days of constant darkness, while 7 days of constant darkness led to a significant reduction in the number of proliferating NSCs (Figures 2F and 2G; Table S1). Notably, NSCs are mostly quiescent, with few proliferating NSCs under baseline conditions during the 12-h/12-h light/dark cycle, such that a further decrease is difficult to detect and may hence require a longer inhibition time as during 7 days of darkness. To overcome this, we took an opposite approach and maintained mice in constant 250-lux light for 3 or 7 days. Indeed, this resulted in a 2.5- and 4-fold increase in the percentage of Ki67$^+$ proliferating NSCs in the SVZ,

Please cite this article in press as: Gengatharan et al., Adult neural stem cell activation in mice is regulated by the day/night cycle and intracellular calcium dynamics, Cell (2021), https://doi.org/10.1016/j.cell.2020.12.026

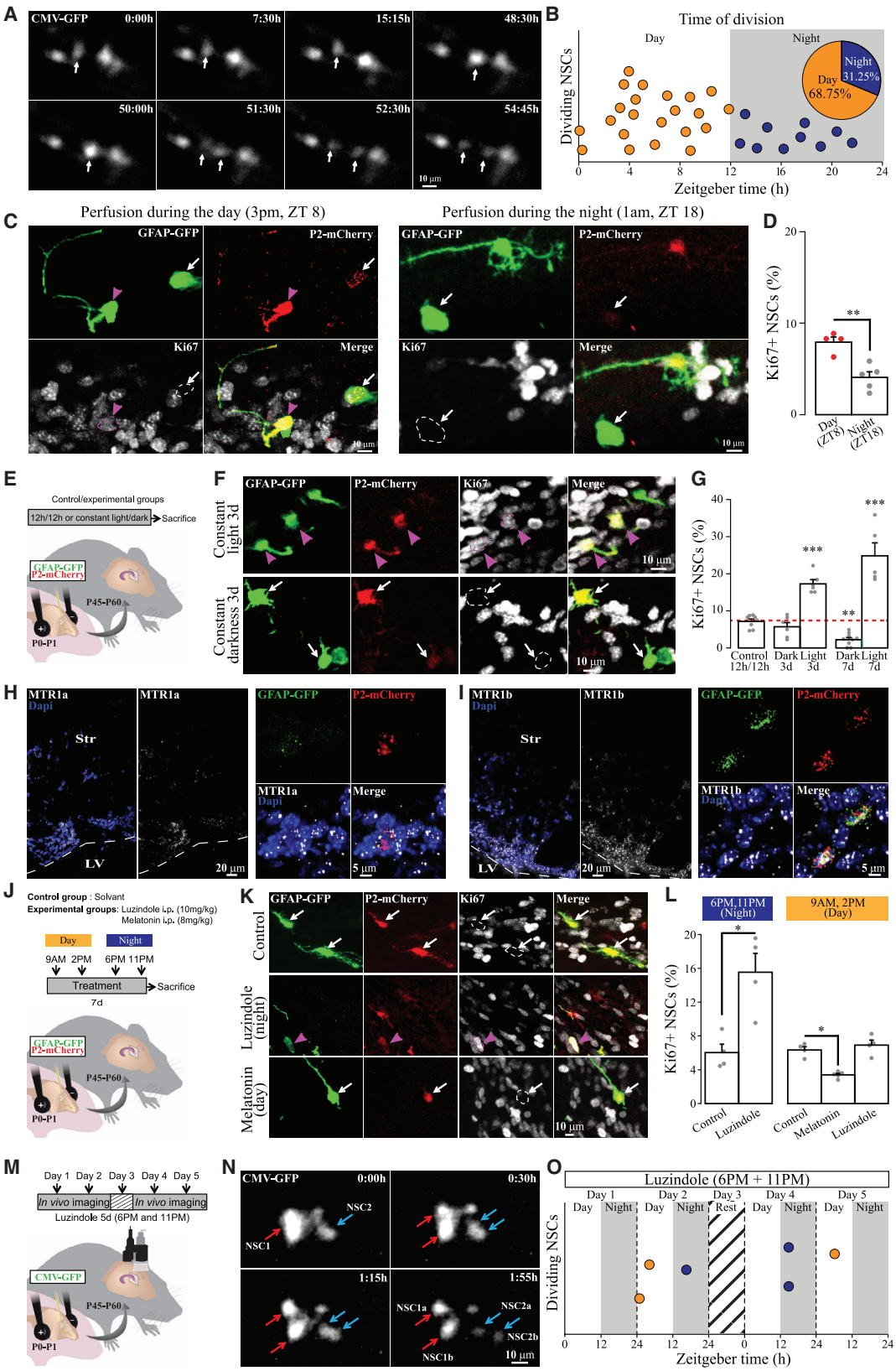

(legend on next page)

Please cite this article in press as: Gengatharan et al., Adult neural stem cell activation in mice is regulated by the day/night cycle and intracellular calcium dynamics, Cell (2021), https://doi.org/10.1016/j.cell.2020.12.026

respectively (Figures 2F and 2G; Table S1). To determine whether the increased proliferation of NSCs reflects a shorter G0 phase or the recruitment of more NSCs into cycle, we performed clustering analysis by monitoring the position of aNSCs relative to each other. Our data revealed only few clusters, suggesting that constant 250-lux induces NSC activation. Altogether, these data indicate that the day/night cycle has a marked impact on NSC activation.

To identify the mechanisms involved in this NSC activation, we focused on melatonin, a circadian hormone that is secreted by the pineal gland in response to darkness (Nakahara et al., 2003) and that inhibits the proliferation of cancer cells and tumor growth (Blask et al., 2002). Melatonin secretion is bimodal, with a first peak at the day/night transition and a second larger peak around midnight (Nakahara et al., 2003). To determine whether NSC division is regulated by melatonin signaling, we first used RNAscope *in situ* hybridization for MTR1a and MTR1b, the G-protein coupled receptors (GPCRs) of melatonin. Interestingly, the two receptors were expressed at higher levels in the SVZ than in the striatum (Figures 2H and 2I). In the SVZ, nearly all cells labeled with DAPI expressed the MTR1a and MTR1b receptors (Figures 2H and 2I). To determine whether NSCs also express these receptors, we performed multiplex RNAscope *in situ* hybridization for GFP, mCherry, and MTR1a or MTR1b on adult mice electroporated with the GFAP-GFP and P2-mCherry plasmids at P0–P1. Our analysis revealed that, like other cells in the SVZ, NSCs express these GPCRs (Figures 2H and 2I). Encouraged by the expression of melatonin receptors on NSCs, we proceeded to functional experiments and blocked their activity using luzindole, a nonselective inhibitor of MTR1a and MTR1b. Adult mice electroporated at P0–P1 with the GFAP-GFP and P2-mCherry plasmids received two injections of luzindole for 7 days at 6 p.m. and 11 p.m., i.e., 1 h before each melatonin secretion peak (Figure 2J). Immunolabeling for Ki67 revealed that luzindole increases the number of proliferative NSCs in the SVZ (Figures 2K and 2L; Table S1). Conversely, the same injection paradigm of luzindole twice a day for 7 days had no effect on the number of Ki67$^+$ proliferating NSCs when the injections were performed during the day (Figure 2L; Table S1) (i.e., at 9 a.m. and 2 p.m., when melatonin levels are low; Nakahara et al., 2003). To increase melatonin levels during the daytime, we injected melatonin at 9 a.m. and 2 p.m. for 7 days, which resulted in the expected decrease in the activation of NSC compared to control DMSO-injected mice (Figures 2K and 2L; Table S1). To determine whether melatonin signaling also affects the dynamics of NSC division in freely behaving mice, we installed mini-endoscopes in adult mice electroporated with the CMV-GFP plasmid at P1. We performed *in vivo* imaging of NSCs following luzindole injections twice a day at 6 p.m. and 11 p.m. for 5 days (Figure 2M). In these experiments, two 48-h sessions of continuous NSC imaging were performed (1 image every 15 min). The two sessions were interrupted by a 24-h rest period during which the NSCs were not imaged. Interestingly, luzindole injections affected the day/night dependence of NSC activation (Figures 2N–2O), with 50% of NSC division occurring during the night (Figure 2O) compared with only 31.25% under baseline conditions (Figure 2B), with no significant changes in the duration of division phase (113.6 ± 13 min, n = 6 cells). These results indicate that day/night regulation of NSC division is mediated by melatonin signaling.

The NSC transition from the quiescent to the proliferative state depends on Ca^{2+} dynamics and steady-state intracellular levels

As neuronal activity regulates NSC physiology (Song et al., 2016) and melatonin affects intracellular Ca^{2+} dynamics (de Faria

Figure 2. NSC division in freely behaving mice is regulated by melatonin during the day/night cycle

(A) Snapshot images showing NSC division in the SVZ of freely behaving mice. NSCs were labeled by the electroporation of the CMV-GFP plasmid at P0–P1. The arrows indicate an NSC undergoing cell division. Note the reduced fluorescent intensity in the daughter cells, which is consistent with the dilution of the plasmid.

(B) A higher propensity for NSC division during the day. The division of NSCs imaged for 2–3 days was plotted against Zeitgeber time (ZT). The inset shows the percentage of NSC division during the day and night.

(C–L) Adult NSCs were labeled by GFAP-GFP and P2-mCherry plasmids electroporated into the SVZ at P0–P1. (C and D) Examples and quantifications of proliferating Ki67$^+$ NSCs during the day (ZT 8) or night (ZT 18). (E) Schematic of the electroporation approach and experimental groups used to determine whether constant light or constant darkness for 3 or 7 days changes the number of aNSCs. The mice were kept either in constant 250-lux light or constant darkness for 3 or 7 days or on a normal 12-h/12-h light/dark cycle. Following anesthesia either in constant darkness or in constant 250-lux light, all the mice in the three groups were perfused from 9 to 11 a.m. (F and G) Examples and aNSC quantification after keeping the mice in a constant light or in constant darkness for 3 or 7 days. (H and I) RNAscope *in situ* hybridization for the MTR1a (H) and MTR1b (I) melatonin receptors in the SVZ. Note the higher expression of these receptors in the SVZ than in the striatum. Multiplex RNAscope *in situ* hybridization for the GFP, mCherry, and MTR1a or MTR1b receptors. (J) Schematic of the electroporation approach and experimental groups used to assess the effect of melatonin receptor activation or inhibition on NSC proliferation. Luzindole, a nonselective inhibitor of the MTR1a and MTR1b receptors, was injected twice a day for 7 days either at 6 p.m. and 11 p.m (night) or at 9 a.m. and 2 p.m. (day). Melatonin was injected twice a day for 7 days at 9 a.m. and 2 p.m. The mice were perfused either at 10 a.m. or 3 p.m. (K and L) Examples and quantification of aNSCs after the 7-day luzindole or melatonin treatments during the day or night.

(M) Schematic of the electroporation and experimental approach used to assess the role of luzindole on NSC activation in freely behaving mice. Luzindole was injected twice a day at 6 p.m. and 11 p.m. for 5 days, and two 48-h sessions of continuous *in vivo* NSC imaging were performed. The two sessions were interrupted by a 24-h rest period.

(N) Snapshot images showing NSCs division in the SVZ of freely behaving mice following the luzindole injections. The red and blue arrows indicate two NSCs undergoing cell division.

(O) A higher propensity for NSC division during the night was observed following the luzindole injections, as compared to the baseline (Figure 2B).

Data are expressed as means ± SEM; n = 32 cells from 16 mice for (B). The number of cells and mice for other experiments are indicated in Table S1. In all the NSC proliferation experiments, we determined the percentage of Ki67$^+$ NSCs with respect to GFP$^+$/mCherry$^+$ cells. The white arrows and ROIs indicate Ki67$^-$ qNSCs, while the magenta arrowheads and ROIs indicate Ki67$^+$ aNSCs. Statistical significance was determined using an unpaired two-sided Student's t test (D), one-way ANOVA followed by a least significant difference (LSD)-Fisher post hoc test (G), or Mann-Whitney *U* test (L). See also Figure S2 and Video S4.

Please cite this article in press as: Gengatharan et al., Adult neural stem cell activation in mice is regulated by the day/night cycle and intracellular calcium dynamics, Cell (2021), https://doi.org/10.1016/j.cell.2020.12.026

Poloni et al., 2011), we next studied the role of intracellular Ca^{2+} signaling in adult NSCs in freely behaving animals. We co-electroporated a genetically encoded Ca^{2+} indicator (GCaMP6s) and a proliferation sensor (geminin$_{1-110}$-mCherry) driven by the GFAP and CMV promoters, respectively, into P0–P1 pups and performed two-color mini-endoscopic imaging in adulthood (Figure 3A). Intriguingly, GFAP-GCaMP6s$^+$/geminin$^+$ aNSCs displayed a significantly lower frequency and amplitude of Ca^{2+} transients than GFAP-GCaMP6s$^+$/geminin$^-$ cells (Figures 3B–3D; Table S2). As GFAP-GCaMP6s$^+$/geminin$^-$ cells may be niche astrocytes or quiescent NSCs (qNSCs), we performed 1-h Ca^{2+} imaging (one acquisition every 30 s) of GFAP-GCaMP6s$^+$ cells in acute brain slices containing the SVZ followed by fixing and immunostaining for s100β and PCNA (Figures S2 and S3). This post hoc immunolabeling made it possible to distinguish and accurately assess Ca^{2+} dynamics in NSCs (Figures 3E–3G and S3) or niche astrocytes (Figure S2). Our experiments confirmed that the transition from the quiescent (s100β$^-$/PCNA$^-$) to the proliferative (s100β$^-$/PCNA$^+$) state of NSCs is associated with a reduced frequency and amplitude of Ca^{2+} transients (Figures 3E–3G; Table S2; Video S5). The same results were obtained using the dual labeling strategy for NSCs electroporated at P0–P1 with the GFAP-GCaMP6s and P2-mCherry plasmids followed in adulthood by Ca^{2+} imaging in slices and post hoc immunostaining for Ki67 (Figures 3H–3J and S3; Table S2). These data further confirmed that qNSCs and aNSCs exhibit different Ca^{2+} dynamics, with a higher frequency and amplitude in qNSCs. To rule out any effect of long-term buffering of Ca^{2+} by GCaMP6s on NSC physiology, we performed experiments with an organic Ca^{2+} indicator (Rhod2-AM) in bromodeoxyuridine (BrdU)-label-retaining cells in GFAP-GFP mice followed by post hoc identification of imaged cells and again observed a difference in Ca^{2+} transients between qNSCs and aNSCs (Figure S3).

In addition to the distinct frequency and amplitude of spontaneous Ca^{2+} events in qNSCs and aNSCs, we also observed higher basal fluorescence of the GCaMP6s signal in aNSCs *in vivo* and in slices, hinting at different cytosolic levels of intracellular Ca^{2+} in qNSCs and aNSCs (Figures 3B, 3E, 3F, 3H, and 3I; Video S5). Indeed, the ratiometric Ca^{2+} indicator Twitch-2B (Thestrup et al., 2014), driven by the GFAP promoter, revealed that there are higher steady-state cytosolic intracellular Ca^{2+} levels in aNSCs than in qNSCs (Figures 3K–3M; Table S2). Taken together, our results show that Ca^{2+} dynamics and cytosolic levels change markedly in adult NSCs during their transition from the quiescent to the proliferative state.

Melatonin signaling modulates Ca^{2+} dynamics and steady-state intracellular levels in NSCs

Our *in vivo* imaging data demonstrated that NSC division is under the control of day/night cycle and that inhibiting melatonin signaling increases NSC proliferation (Figure 2). Given the differences in Ca^{2+} dynamics and steady-state intracellular levels in qNSCs and aNSCs, we performed Ca^{2+} imaging in acute brain slices to determine whether the increase in proliferative NSCs when MTRs are blocked is linked to Ca^{2+} signaling. Prior to this, we first determined the reliability of the acute slice preparation with respect to melatonin levels by applying the inhibitor luzindole at different concentrations for 3 h to acute slices from P45–P60 mice that had received the GFAP-GFP and P2-mCherry plasmids at P0–P1. The acute slices were prepared at 1–2 a.m., when melatonin levels are high (Nakahara et al., 2003). *Post hoc* immunolabeling for Ki67 revealed a 3- to 4-fold increase in the number of proliferating Ki67$^+$ NSCs (Figures 4A and 4B), which is consistent with our *in vivo* data (Figure 2L). We next prepared acute brain slices from adult mice at the same time (1–2 a.m.) that had been electroporated at P0–P1 with GFAP-GCaMP6s and performed Ca^{2+} imaging under baseline conditions and following application of luzindole (15 μM) (Figure 4C). To minimize potential melatonin washout in the acute brain slices by the 1–2 mL/min flow rate of artificial cerebrospinal fluid (ACSF), we performed imaging only for 20–25 min (10 min at baseline followed by 10–15 min in the presence of luzindole, with one acquisition every 10 s). The Ca^{2+} imaging was followed by post hoc identification of qNSCs and aNSCs by immunostaining for PCNA and s100β. Interestingly, luzindole decreased the frequency of Ca^{2+} fluctuations in qNSCs (Figure 4D; Video S6). To investigate whether blocking MTRs also increases cytosolic Ca^{2+} levels *in vivo*, we electroporated mice with GFAP-Twitch2B and P2-mCherry at P0–P1 and injected luzindole i.p. in adulthood twice a day at 6 p.m. and 11 p.m. for 7 days (Figure 4E). The luzindole injections increased the steady-state intracellular levels of Ca^{2+} in qNSCs, but not in aNSCs (Figures 4F and 4G). This showed that luzindole-mediated changes in NSC activation in acute brain slices (Figures 4A and 4B) and *in vivo* (Figures 2K–2L) are linked to modifications in intracellular Ca^{2+} levels and the frequency of Ca^{2+} fluctuations observed both *in vivo* and *ex vivo* (Figures 4C–4G).

EGF affects Ca^{2+} dynamics and steady-state intracellular levels in NSCs

We next aimed to compare the novel role of luzindole in affecting NSC proliferation and Ca^{2+} levels and dynamics to well-known stimulators of NSC division, such as epidermal growth factor (EGF), a highly potent pro-proliferative factor that triggers NSC and progenitor division (Doetsch et al., 2002; Joppé et al., 2015). We performed Ca^{2+} imaging for 1 h under baseline conditions and following a 1-h application of EGF (0.1 μg/mL) in adult brain slices from mice electroporated at P0–P1 with the GFAP-GCaMP6 plasmid (Figure 5A) followed by a post hoc identification of qNSCs and aNSCs as described above (Figures 5B and S3). Consistent with the effects of luzindole, EGF decreased the frequency and amplitude of Ca^{2+} signals in qNSCs (Figures 5C and 5D; Video S7) and further lowered the frequency of Ca^{2+} signals in aNSCs, with no change in the amplitude (Figures 5C and 5D). To determine whether EGF also affects intracellular Ca^{2+} levels, we incubated adult brain slices from mice electroporated at P0–P1 with the GFAP-Twitch2B plasmid with EGF followed by a post hoc identification of qNSCs and aNSCs. This incubation led to an increase in intracellular Ca^{2+} levels in qNSCs, but not in aNSCs (Figures 5E and 5F). To ensure that the observed changes in Ca^{2+} dynamics and cytosolic levels were linked to an increased proliferation of NSCs, we incubated acute brain slices from adult mice that had been electroporated with GFAP-GFP and P2-mCherry plasmids at P0–P1 in EGF (0.1 μg/mL) for 3 h. As expected, this increased the number of proliferative NSCs (Figures 5G and 5H). These data and previous reports

Please cite this article in press as: Gengatharan et al., Adult neural stem cell activation in mice is regulated by the day/night cycle and intracellular calcium dynamics, Cell (2021), https://doi.org/10.1016/j.cell.2020.12.026

CellPress

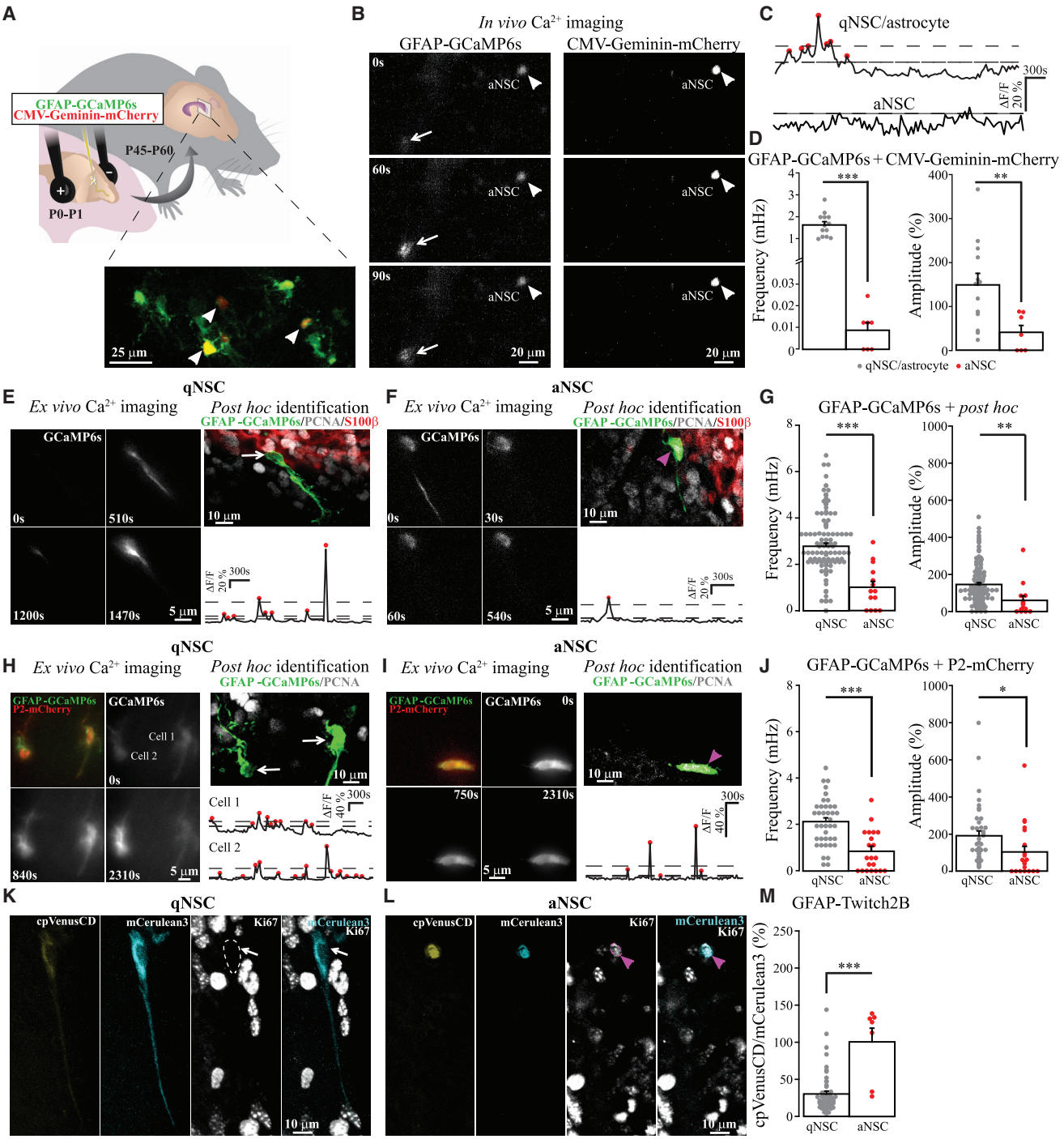

Figure 3. qNSCs and aNSCs display different Ca^{2+} dynamics

(A and B) Schematic showing the electroporation of GFAP-GCaMP6s and CMV-geminin-mCherry at P0–P1, and an image showing labeled cells in the SVZ. (B–D) Ca^{2+} activity in an aNSC (arrowhead) and in a GFAP-GCaMP6s$^+$ cell (arrow), sample traces, and quantification of Ca^{2+} activity in freely behaving mice. (E–G) Examples of Ca^{2+} activity in qNSCs and aNSCs in acute brain slices and quantification of the frequency and amplitude of Ca^{2+} events in these cells. (H–J) Quantification of the frequency and amplitude of Ca^{2+} events in qNSCs and aNSCs defined by the coincident activity of the GFAP and P2 promoters. (K–M) Measurement of cytosolic Ca^{2+} levels in qNSCs and aNSCs using the Twitch-2B ratiometric Ca^{2+} indicator.

Data are expressed as means ± SEM. The individual values of all experiments are also shown. The exact value of *n* and its representation (cells, animals) for the experiments is indicated in Table S2. The white arrows and ROI indicate Ki67- qNSCs while the magenta arrowheads and ROI indicate Ki67$^+$ aNSCs. Statistical significance was determined using an unpaired two-sided Student's t test or a Mann-Whitney *U* test for the experiments described in (M). See also Figures S2 and S3 and Video S5.

Please cite this article in press as: Gengatharan et al., Adult neural stem cell activation in mice is regulated by the day/night cycle and intracellular calcium dynamics, Cell (2021), https://doi.org/10.1016/j.cell.2020.12.026

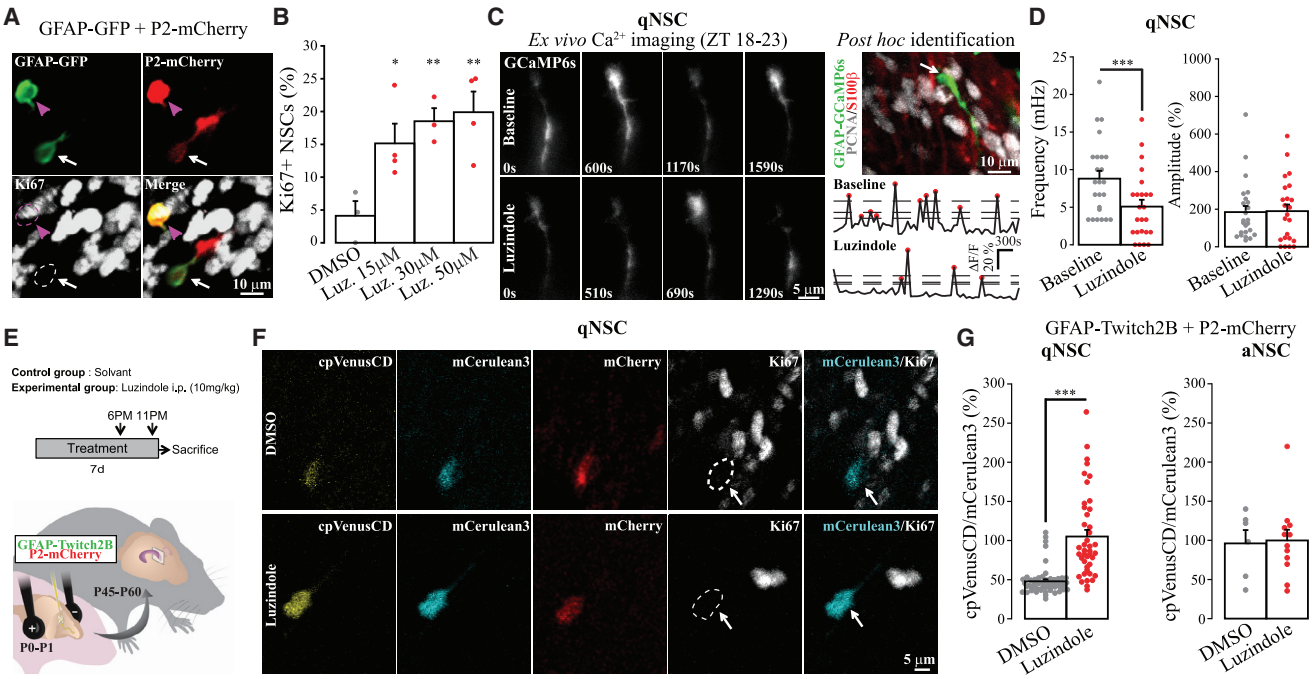

Figure 4. The luzindole-induced increase in NSC proliferation is linked to changes in Ca^{2+} dynamics and steady-state cytosolic levels

(A) Immunolabeling of acute brain slices with Ki67 following a 3-h incubation with luzindole, a nonselective inhibitor of the MTR1a and MTR1b receptors. The acute brain slices were prepared at 1–2 a.m. from mice that had been electroporated with GFAP-GFP and P2-mCherry at P0–P1.

(B) Quantification of the number of aNSCs following a 3-h incubation with luzindole at different concentrations.

(C) Ca^{2+} imaging in acute adult brain slices under baseline conditions (upper panel) and following the application of luzindole (lower panel). The post hoc identification of imaged cells was performed by PCNA and s100β immunolabeling (right panel). The acute brain slices were prepared at 1–2 a.m., and Ca^{2+} imaging was performed from 2 to 6 a.m.

(D) Quantification of the frequency and amplitude of Ca^{2+} events in qNSCs under baseline conditions and following the application of luzindole.

(E) Schematic drawing of the experimental approach used to test the impact of MTRs inhibition on cytosolic Ca^{2+} levels.

(F and G) Example and quantification of cytosolic Ca^{2+} levels in qNSCs and aNSCs *in vivo* following i.p. injections of luzindole twice a day at 6 p.m. and 11 p.m. for 7 days. The mice had previously been electroporated with GFAP-Twitch2B and P2-mCherry.

Data are expressed as means ± SEM. The individual values of all the experiments are also shown. The exact value of *n* and its representation (cells, animals) is indicated in Table S2. The white arrows and ROIs indicate $Ki67^-$ qNSCs, while the magenta arrowheads and ROI indicate $Ki67^+$ aNSCs. The one-way ANOVA followed by LSD-Fisher post hoc analysis was used for the experiments described in (B), a paired Student's t test was used for the experiments described in (D) (as the same cells were imaged under baseline conditions and following the application of luzindole), and an unpaired Student's t test was used in (G). See also Video S6.

showing that EGF increases the proliferation of NSCs (Doetsch et al., 2002; Joppé et al., 2015) imply that EGF receptors are already expressed in qNSCs. To test this hypothesis, we sorted qNSCs and aNSCs from the SVZ of GFAP-GFP mice based on the expression of GFP, CD133 (prominin), and EGFR (Beckervordersandforth et al., 2010; Fischer et al., 2011) and performed RNA sequencing (RNA-seq) analysis. We detected EGFR transcripts in qNSCs, albeit at lower levels than in aNSCs (Figure S4). Altogether, our results suggest that the intracellular Ca^{2+} levels and dynamics of NSCs are modulated by pro-proliferative factors such as EGF in a way similar to the effects observed when luzindole blocks melatonin receptors.

IP3-sensitive intracellular stores control different Ca^{2+} dynamics during the NSC transition from quiescence to proliferation

Melatonin receptors are GPCRs, while EGF binds to receptor tyrosine kinase receptors. These two receptor families regulate Ca^{2+} levels and the frequency of Ca^{2+} fluctuations by various mechanisms (de Faria Poloni et al., 2011; Hodeify et al., 2018). Accordingly, both melatonin and EGF have been shown to influence Ca^{2+} release from internal stores (Bach et al., 2005; Pecenin et al., 2018; Tinhofer et al., 1996). To explore the role of internal stores in determining Ca^{2+} dynamics and levels during the NSC transition from quiescence to proliferation, we first used 2APB (100 µM), which blocks Ca^{2+} release from IP3-sensitive intracellular stores, and thapsigargin (3 µM), which inhibits sarco/endoplasmic reticulum Ca-ATPase (SERCA). Ca^{2+} imaging of GFAP-GCaMP6s-electroporated cells before and after the pharmacological treatments was followed by the post hoc identification of qNSCs and aNSCs, as described above (Figures 6A, 6B, and S3). Our results showed that both 2APB and thapsigargin decrease the frequency of Ca^{2+} events and increase cytosolic Ca^{2+} levels in qNSCs, but not in aNSCs (Figures 6C–6E; Table S2). Importantly, these changes in Ca^{2+} dynamics and levels increased the proliferation of NSCs (Figure 6F), indicating

Please cite this article in press as: Gengatharan et al., Adult neural stem cell activation in mice is regulated by the day/night cycle and intracellular calcium dynamics, Cell (2021), https://doi.org/10.1016/j.cell.2020.12.026

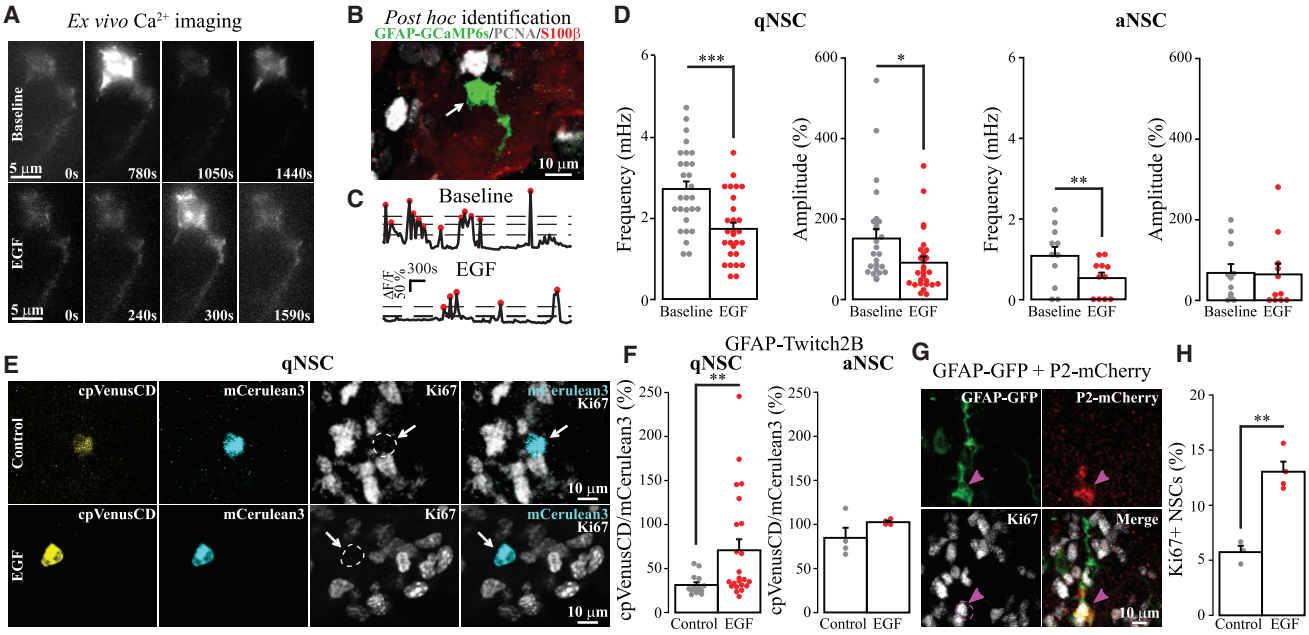

Figure 5. EGF affects Ca^{2+} dynamics and steady-state intracellular levels in NSCs

(A–D) Example of Ca^{2+} imaging in acute adult brain slices and quantification of the frequency and amplitude of Ca^{2+} events in qNSCs and aNSCs under baseline conditions and following the application of EGF (0.1 µg/mL).

(E and F) Example and quantification of cytosolic Ca^{2+} levels in qNSCs and aNSCs following the application of EGF (0.1 µg/mL).

(G and H) Examples and quantification of the number of proliferative NSCs following a 3-h incubation with EGF. The acute brain slices were prepared from adult mice that had been electroporated with the GFAP-GFP and P2-mCherry plasmids at P0–P1.

Data are expressed as means ± SEM. The individual values of all experiments are also shown. The exact value of *n* and its representation (cells, animals) is indicated in Tables S1 and S2. The white arrows and ROIs indicate $Ki67^-$ qNSCs, while the magenta arrowheads and ROI indicate $Ki67^+$ aNSCs. Statistical significance was determined using a paired Student's t test for (D), as the same cell was imaged under baseline conditions and following the application of EGF. A Mann-Whitney *U* test was used for the experiments described in (F), and an unpaired Student's t test was used for the experiments described in (H). See also Figure S4 and Video S7.

that they play a functional role in NSC activation. No changes were observed following the blocking of the NMDA, TrpC, or TrpV4 channels (Figure 6C).

The drawback of the pharmacological approach is the lack of cell specificity, as it affects all cells in a slice. To address this limitation, we used CRISPR-Cas9 to delete *Itpr2*, the receptor that regulates the release of Ca^{2+} from internal stores, specifically in SVZ NSCs, by co-electroporating a plasmid encoding a gRNA that targets *Itpr2*, Cas9, and mCherry under the P2 promoter (pU6-gRNA-P2-Cas9-T2A-mCherry) with GFAP-GFP or GFAP-GCaMP6 (Figures S3 and S4) and monitored Ca^{2+} activity specifically in these double-labeled NSCs. Deleting *Itpr2* in NSCs decreased the frequency of Ca^{2+} events in qNSCs (Figures 6G–6I; Table S2) and led to the entry of qNSCs into the proliferative state (Figures 6J and 6K; Table S1). Importantly, this increase in NSC proliferation was sustained for several weeks as we detected a higher number of aNSCs at 10 and 60 days post-electroporation *in vivo* (Figure 6K). It is worth noting that we assess acutely dividing cells when monitoring Ki67. The data indicate that there was a 2-fold increase in acutely dividing NSCs at any given moment from P10 to P60, and thus, the total increase in NSC proliferation over the entire period should be cumulative and hence in total much higher. Taken together, these results show that there is a causal relationship between internal store-dependent Ca^{2+} dynamics in NSCs and their transition from the quiescent to the proliferative state.

In vivo optogenetic maintenance of the Ca^{2+} dynamics of qNSCs inhibits their transition to the proliferative state

The results reported above showed that the deletion of *Itpr2* or 3 days of constant 250-lux light increase the number of proliferating NSCs *in vivo*. It remains unclear, however, whether the modulation of Ca^{2+} dynamics alone can reverse the transition of NSCs from the quiescent to the proliferative state. To directly regulate Ca^{2+} dynamics in NSCs of freely behaving mice *in vivo*, we optogenetically manipulated Ca^{2+} dynamics using hBACCS2, a light-inducible actuator that allows the entry of Ca^{2+} via ORAI channels (Ishii et al., 2015). We first made sure that the optogenetic activation of hBACCS2 induces Ca^{2+} entry into adult SVZ cells. To do so, we electroporated mice with GFAP-hBACCS2-IRES-GFP at P0–P1, prepared acute brain slices at P45–P60, and loaded the slices with the Rhod2-AM organic Ca^{2+} indicator (Figure 7A). Ca^{2+} activity was imaged under baseline conditions and following a single 60-s optogenetic stimulation at 488 nm. This showed that the light-induced stimulation of GFAP-hBACCS2$^+$ cells increases Rhod2 fluorescent intensity in these cells (Figure 7B). After validating this construct, we proceeded to *in vivo* experiments by co-electroporating

Please cite this article in press as: Gengatharan et al., Adult neural stem cell activation in mice is regulated by the day/night cycle and intracellular calcium dynamics, Cell (2021), https://doi.org/10.1016/j.cell.2020.12.026

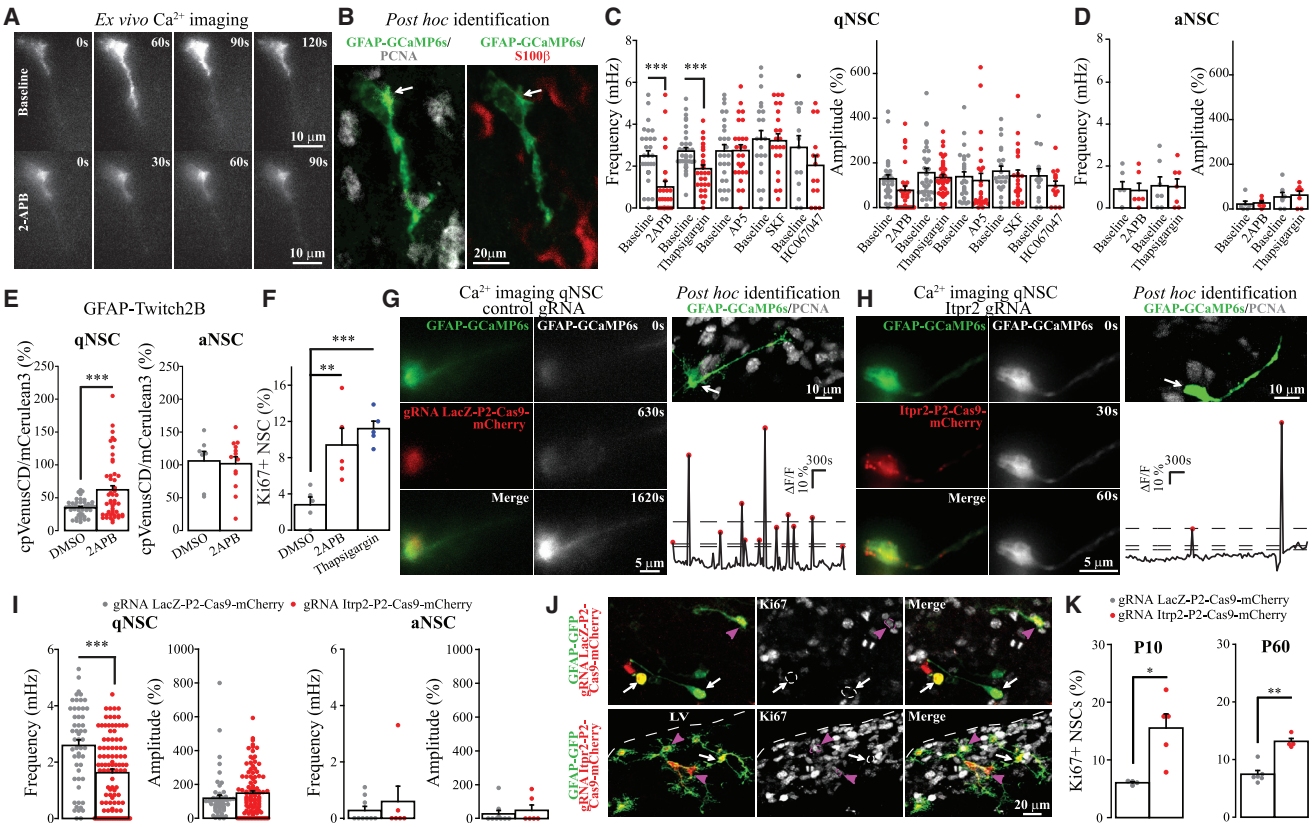

Figure 6. Ca^{2+} dynamics in NSCs depend on IP3-sensitive intracellular stores

(A–D) Example of Ca^{2+} imaging in acute adult brain slices and quantification of the frequency and amplitude of Ca^{2+} events in qNSCs and aNSCs under baseline conditions and following the application of different pharmacological compounds.

(E) Quantification of cytosolic Ca^{2+} levels in qNSCs and aNSCs following an incubation with 2APB.

(F) Quantification of the number of aNSCs following a 3-h incubation with 2APB or thapsigargin.

(G–I) Examples of Ca^{2+} activity in qNSCs and aNSCs and quantification of the frequency and amplitude of Ca^{2+} events in these cells when *Itpr2* expression is affected.

(J) Increased proliferation of NSCs when *Itpr2* expression is affected.

(K) Quantification of proliferative NSCs following the deletion of *Itpr2* in P10 and P60 mice.

Data are expressed as means ± SEM. The individual values of all experiments are also shown. The exact value of n and its representation (cells, animals) is indicated in Tables S1 and S2. The white arrows and ROIs indicate $Ki67^{-}$ qNSCs, while the magenta arrowheads and ROIs indicate $Ki67^{+}$ aNSCs. Statistical significance was determined using a paired Student's t test for all the pharmacological experiments, as the same cell was imaged under baseline conditions and following the application of the different pharmacological compounds. An unpaired Student's t test was used for the experiments described in (E) and (I) and a Mann-Whitney *U* test for (K). The one-way ANOVA followed by LSD-Fisher post hoc test was used for the experiments described in (F). See also Figures S3 and S4.

GFAP-hBACCS2-IRES-GFP (or GFAP-GFP as a control) together with *Itpr2* gRNAs and Cas9 under the P2 promoter at P0–P1 and installing two optical fibers in the lateral ventricle at P60–P90 to cover the entire medio-lateral portion of the SVZ (Figures 7C and S5). To compensate for the 2-fold reduction in the Ca^{2+} frequency induced by the *Itpr2* deletion in qNSCs, we optogenetically stimulated NSCs with five or six pulses per hour for 3 days. Light-induced Ca^{2+} entry into NSCs for 3 days restored the changes in proliferation induced by *Itpr2* gene editing (Figures 7D and 7E; Table S1). Importantly, no effects were observed in the two control groups, one of which received no stimulation and one of which was optogenetically stimulated but did not receive the hBACCS2 construct (Figures 7D and 7E; Table S1).

As NSC activation was also regulated by the day/night cycle (Figure 2) through melatonin signaling-mediated changes in Ca^{2+} dynamics and levels (Figure 4), we determined whether optogenetically induced Ca^{2+} entry into NSCs would also restore the 3-day constant 250-lux light-induced increase in NSC proliferation. We thus co-electroporated GFAP-hBACCS2-IRES-GFP (or GFAP-GFP as a control) together with P2-mCherry at P0–P1 and installed two optical fibers in the lateral ventricle in adulthood (Figure 7F). We kept the mice in constant 250-lux light for 3 days and at the same time optogenetically stimulated the NSCs as described above. Interestingly, optogenetically induced Ca^{2+} entry into NSCs also reverted the constant light-induced transition to the proliferative state (Figures 7G and 7H). Altogether, our experiments demonstrate that there is a

Please cite this article in press as: Gengatharan et al., Adult neural stem cell activation in mice is regulated by the day/night cycle and intracellular calcium dynamics, Cell (2021), https://doi.org/10.1016/j.cell.2020.12.026

CellPress

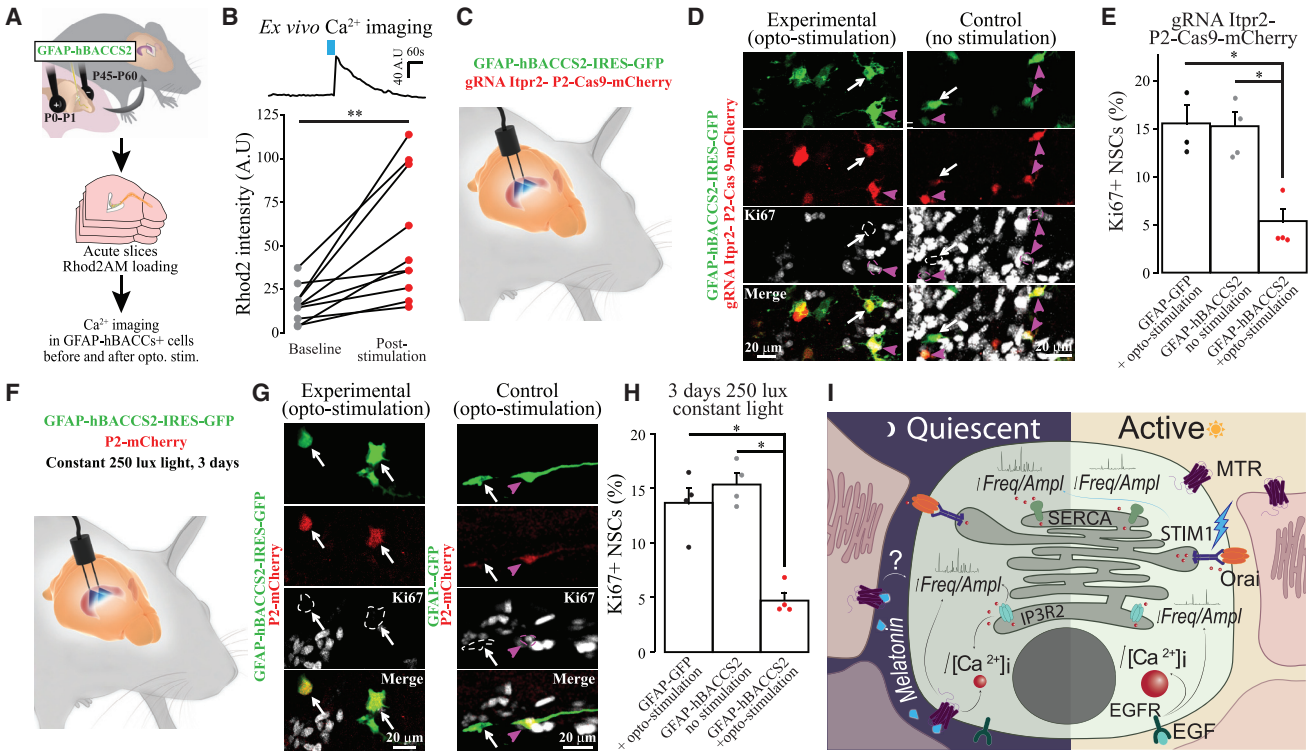

Figure 7. *In vivo* optogenetic restoration of Ca^{2+} dynamics in NSCs reverses their transition to the proliferative state

(A) Schematic showing the electroporation of GFAP-hBACCS2-IRES-GFP at P0–P1 followed by loading cells in acute brain slices with Rhod2-AM.

(B) Quantification of Rhod2 fluorescent intensity before and after a single 488-nm light pulse to induce Ca^{2+} entry.

(C) Schematic showing the location of the optical fibers used for the optogenetic stimulation of NSCs.

(D and E) Images and quantification of NSC proliferation when *Itpr2* expression is affected combined with the optogenetic stimulation of Ca^{2+} entry into NSCs to mimic the Ca^{2+} dynamics of the quiescent state.

(F) Schematic showing the electroporated plasmids and experimental conditions for the optogenetic stimulation of NSCs activated by 250-lux constant light for 3 days.

(G and H) Images and quantification of the number of $Ki67^+$ NSCs under different conditions.

(I) Schematic showing different intracellular Ca^{2+} pathways regulating the NSC transition from quiescence to proliferation.

Data are expressed as means ± SEM. The individual values of all the experiments are also shown. The exact value of n and its representation (cells, animals) is indicated in Table S1. The white arrows and ROIs indicate $Ki67^-$ qNSCs, while the magenta arrowheads and ROIs indicate $Ki67^+$ aNSCs. Statistical significance was determined using a paired Student's t test for (B) and Mann-Whitney *U* test for (E) and (H). See also Figure S5.

causal link between Ca^{2+} signaling and NSC activation (Figure 7I) and reveal the key role played by subtype-specific Ca^{2+} dynamics in qNSCs, which is sufficient to maintain the quiescent state even after promoting their transition to the activated state by prolonged daylight exposure or *Itpr2* deletion.

DISCUSSION

Live imaging reveals the day/night-dependent and melatonin-mediated kinetics of NSC activation in freely behaving mice

Here, we provide the live *in vivo* imaging of NSCs in freely behaving mice monitoring their activation and division which led to two major new discoveries: their activation is biased to the beginning of the daylight time and is accompanied by changes in Ca^{2+} dynamics and intracellular steady-state levels.

Live imaging of adult NSCs has already led to major insights, such as the discovery of the direct conversion of NSCs into neurons in the zebrafish forebrain and the discovery of self-renewing transit-amplifying daughter cells in the dentate gyrus (Barbosa et al., 2015; Pilz et al., 2018). However, in addition to the possible side effects of immobilization or anesthesia, certain aspects of NSC physiology can only be studied by continuous (every 15 min) imaging in freely behaving mice. One issue that could not be addressed previously is when NSC activation occurs over one or more 24-h cycles, as imaging could not be performed continuously for several days in animals that naturally explore their environment and go through several 24-h cycles. We used advanced mini-endoscopic imaging and observed a striking 70% bias toward NSC division during the daylight period. We corroborated these findings by demonstrating that constant light conditions as well as blocking MTR1a and MTR1b by luzindole during the night increase NSC activation and division, whereas constant darkness or stimulating MTR1a and MTR1b with melatonin during the day decrease NSC activation. Thus, the hormone melatonin, which is released in response

Please cite this article in press as: Gengatharan et al., Adult neural stem cell activation in mice is regulated by the day/night cycle and intracellular calcium dynamics, Cell (2021), https://doi.org/10.1016/j.cell.2020.12.026

to darkness (Nakahara et al., 2003), inhibits NSC activation, shifting NSC division in large part to the daylight period.

Interestingly, clock genes that regulate circadian rhythms have been shown to regulate stem cell behavior in other organs (Benitah and Welz, 2020; Plikus et al., 2013; Samsa et al., 2016) as well as progenitor proliferation in the adult dentate gyrus (Bouchard-Cannon et al., 2013). The lack of PERIOD2 abolishes the entry of progenitor cells into the cell cycle, while the genetic ablation of BMAL1 delays the exit of dentate gyrus progenitor cells from the cell cycle (Bouchard-Cannon et al., 2013). It remains unclear, however, which signals integrate stem cell activation with circadian rhythms and animal behavior. This has particular relevance for NSCs, since brain neural networks govern animal behavior. Our data provide information on how external stimuli regulate the day/night activity of NSCs. Since mice are nocturnal animals, this also raised the interesting possibility that NSC division may be regulated by the sleep/wake cycle. Future experiments correlating NSC imaging using mini-endoscopes and REM and non-REM sleep recordings will be required to address this issue. It should be noted, however, that melatonin release is induced by darkness in both nocturnal and diurnal animals (Macchi and Bruce, 2004), indicating that the inhibitory effects of melatonin on NSC activation observed in our study should occur independently of the sleep/wake state of the animals. However, additional signals may be superimposed on the regulation of NSC activation during the sleep/wake cycle. It would thus be interesting to assess NSC division in both diurnal and nocturnal animals. This would shed light on the possible complex interplay between regulatory factors that operate during the day/night and sleep/wake cycles and how combination of these factors modulates NSC activity.

It also remains so far unclear whether melatonin-induced modulation of NSC proliferation is cell autonomous or is triggered by the activation of other cell types in the SVZ that also express these receptors and signal to NSCs to modulate their transition from the quiescent to the proliferative state. Future studies using NSC-specific gene editing for MTR1a and MTR1b may help addressing this issue. Interestingly, hunger and satiety regulate NSC activation via axonal projections from hypothalamic proopiomelanocortin neurons that converge in the ventral SVZ (Paul et al., 2017). As these are also subject to circadian rhythms (Challet, 2019), day/night signaling may be upstream and may contribute to the hunger- and satiety-induced activation of NSCs. Importantly, the NSC imaging technology developed in the present study now makes it possible to investigate how NSC function adapts in response to different behavioral states.

Ca^{2+} as an integrator and decoder of microenvironmental signals governing NSC activation

The second major advance in the present study is that our *in vivo* analysis of Ca^{2+} dynamics and intracellular levels in NSCs unraveled a general mechanism of NSC activation. Our results showed that not only are the quiescent and proliferative states of NSCs determined by striking differences in intracellular Ca^{2+} dynamics and steady-state cytosolic levels but also that changes in Ca^{2+} dynamics and steady-state cytosolic levels drive NSC behavior *in vivo*. We uncovered a Ca^{2+} signature of quiescent and active NSCs and showed that qNSCs exhibit a higher frequency and amplitude of Ca^{2+} events but lower cytosolic Ca^{2+} levels than aNSCs. Our results further showed that several signaling pathways converge on Ca^{2+} to regulate the NSC transition from quiescence to proliferation. Inhibiting the quiescence-associated melatonin signaling pathway activates NSCs by reducing the frequency of Ca^{2+} fluctuations and increasing intracellular Ca^{2+} levels, and potentiating NSC division by EGF, a well-known factor that activates NSCs (Doetsch et al., 2002; Joppé et al., 2015), affects Ca^{2+} dynamics and levels in the same manner. We also unraveled the signaling mechanisms underlying these different Ca^{2+} dynamics and showed that IP3-sensitive intracellular stores sustain Ca^{2+} signaling in the quiescent state. Interestingly, both EGFR and MTR1 activity affect mitogen-activated protein kinase (MAPK) signaling, while MTRs inhibits it (Blask et al., 2002) and EGFR activates it (Avraham and Yarden, 2011). Both signaling pathways also affect intracellular Ca^{2+} levels via IP3-sensitive intracellular stores (de Faria Poloni et al., 2011; Hodeify et al., 2018), supporting the concept that the frequency of Ca^{2+} signals may act as an integrator and decoder of various signals that then mediate the transition of NSCs from the quiescent to the active state (Figure 7I). Recent observations showing that fluid flow promotes the proliferation of SVZ progenitors via the epithelial sodium-channel-dependent activation of Ca^{2+}-release activated channels (CRAC) and ERK phosphorylation (Petrik et al., 2018) are also in line with this concept. Altogether, these results suggest that microenvironmental signals involved in the day/night, mitogenic, and cerebrospinal-fluid-induced regulation of NSCs converge on intracellular Ca^{2+} signaling pathways to mediate NSC quiescence and proliferation.

Interestingly, similar Ca^{2+} dynamics have been observed in gut and skin somatic stem cells (Deng et al., 2015; He et al., 2018; Horsley et al., 2008) as well as in embryonic and hematopoietic stem cells *in vitro* (Luchsinger et al., 2019; MacDougall et al., 2019). In gut stem cells, high cytosolic Ca^{2+} levels trigger proliferation, whereas Ca^{2+} oscillations maintain quiescence (Deng et al., 2015; He et al., 2018). These changes in Ca^{2+} dynamics are required to decode metabolic, mechanical, and growth factor signals that balance gut stem cell quiescence and proliferation (Deng et al., 2015; He et al., 2018). However, it was previously difficult to determine whether Ca^{2+} signals simply accompany stem cell activation states or whether they are indeed causative. We showed, using *in vivo* optogenetics, that experimentally modulating Ca^{2+} fluxes into NSCs to mimic their quiescent state is sufficient to reverse their transition to the proliferative state. These data strongly support the concept of Ca^{2+} signaling as the integrator and decoder of multiple signals that determine the activation or quiescence of NSCs.

How do fluctuations in intracellular Ca^{2+} levels trigger changes in NSC proliferation? Interestingly, IP3 uncaging induces Ca^{2+} fluctuations and stimulates gene expression via NFAT (Li et al., 1998). In addition, changes in intracellular Ca^{2+} levels, in particular via IP_3R, may trigger gene transcription in skin stem cells via the calcineurin/NFAT pathway (Horsley et al., 2008). It has been also shown that gene expression may be dynamically modulated by the frequency of Ca^{2+} fluxes, their amplitude, and their duration (Dolmetsch et al., 1997; Dolmetsch et al., 1998). It remains to be shown how different downstream effectors in NSCs respond

to Ca^{2+} signals of different cytosolic levels, amplitudes, and frequencies to initiate gene expression and the entry of NSCs into the activation phase. Most importantly, however, our data show that Ca^{2+} dynamics and intracellular steady-state levels are a key mechanism regulating NSC activation in freely behaving mice and are the mediator of profound circadian regulation of NSC activity.

STAR★METHODS

Detailed methods are provided in the online version of this paper and include the following:

- KEY RESOURCES TABLE
- RESOURCE AVAILABILITY
  - Lead contact
  - Material availability
  - Data and code availability
- EXPERIMENTAL MODEL AND SUBJECT DETAILS
- METHOD DETAILS
  - Electroporation
  - Gradient index (GRIN) lens implantation and *in vivo* imaging in freely behaving mice
  - *In vivo* optogenetic stimulation
  - *In vivo* luzindole and melatonin treatments and constant light/darkness conditions
  - BrdU label-retaining protocol
  - Transcriptome analysis of prospectively isolated qNSCs and aNSCs
  - CRISPR target site selection and assembly
  - Immunostaining
  - Time-lapse Ca^{2+} imaging in acute brain slices
  - Ca^{2+} imaging analysis
  - Post hoc identification of imaged cells
  - RNAscope *in situ* hybridization
- QUANTIFICATION AND STATISTICAL ANALYSIS

SUPPLEMENTAL INFORMATION

Supplemental Information can be found online at https://doi.org/10.1016/j.cell.2020.12.026.

ACKNOWLEDGMENTS

We thank Omar Sayed and Aymeric Ferreira for optimizing the MATLAB script for the Ca^{2+} imaging analysis, Jean-Luc Neron at Doric Lenses for modeling the spread of light during optogenetic stimulations *in vivo*, Aymeric Ferreira for help with processing time-lapse mini-endoscopic imaging videos, Alexandre Gauvin at Alexandre Gauvin Digital Solutions for deconvolution of videos of NSC division shown in Video S3, Dr. Denis Faubert at Mass Spectrometry and Proteomics Platform of Institut de recherches cliniques de Montréal (IRCM) for preliminary analysis of melatonin level in the brain tissue using liquid chromatography-tandem mass spectrometry (LS-MS/MS), and Mireille Massouh at MassouhBioMedia for the schematic drawings. This work was supported by a Canadian Institute of Health Research (CIHR) grant to A.S.

AUTHOR CONTRIBUTIONS

A.G., S.M., A.M., and M. Ghareghani performed the electroporations. A.G., A.M., M. Ghareghani, and A.S. performed the *ex vivo* imaging and analyzed the data. A.G. and S.M. performed the *in vivo* optogenetic stimulation and imaging. S.M. and A.S. installed the mini-endoscopes and optic fibers and performed the *in vivo* imaging. M.S. developed CRISPR-Cas9 in NSCs and performed the gRNA cloning and validation as well as the *in situ* hybridization. J.F.-S. and J.N. performed the RNA-seq analyses of sorted cells. M. Götz contributed to the concept and revised the manuscript. A.S. developed the concept and *in vivo* imaging approach and wrote the manuscript.

DECLARATION OF INTERESTS

The authors declare no competing interests.

Received: May 8, 2020
Revised: August 25, 2020
Accepted: December 15, 2020
Published: January 21, 2021

REFERENCES

Akers, K.G., Martinez-Canabal, A., Restivo, L., Yiu, A.P., De Cristofaro, A., Hsiang, H.L., Wheeler, A.L., Guskjolen, A., Niibori, Y., Shoji, H., et al. (2014). Hippocampal neurogenesis regulates forgetting during adulthood and infancy. Science *344*, 598–602.

Anacker, C., and Hen, R. (2017). Adult hippocampal neurogenesis and cognitive flexibility - linking memory and mood. Nat. Rev. Neurosci. *18*, 335–346.

Avraham, R., and Yarden, Y. (2011). Feedback regulation of EGFR signalling: decision making by early and delayed loops. Nat. Rev. Mol. Cell Biol. *12*, 104–117.

Bach, A.G., Wolgast, S., Mühlbauer, E., and Peschke, E. (2005). Melatonin stimulates inositol-1,4,5-trisphosphate and Ca2+ release from INS1 insulinoma cells. J. Pineal Res. *39*, 316–323.

Bakhshetyan, K., and Saghatelyan, A. (2015). Tracking neuronal migration in adult brain slices. Curr. Protoc. Neurosci. *71*, 3.28.21-13.

Barbosa, J.S., Sanchez-Gonzalez, R., Di Giaimo, R., Baumgart, E.V., Theis, F.J., Götz, M., and Ninkovic, J. (2015). Neurodevelopment. Live imaging of adult neural stem cell behavior in the intact and injured zebrafish brain. Science *348*, 789–793.

Beckervordersandforth, R., Tripathi, P., Ninkovic, J., Bayam, E., Lepier, A., Stempfhuber, B., Kirchhoff, F., Hirrlinger, J., Haslinger, A., Lie, D.C., et al. (2010). In vivo fate mapping and expression analysis reveals molecular hallmarks of prospectively isolated adult neural stem cells. Cell Stem Cell *7*, 744–758.

Benitah, S.A., and Welz, P.S. (2020). Circadian regulation of adult stem cell homeostasis and aging. Cell Stem Cell *26*, 817–831.

Blask, D.E., Sauer, L.A., and Dauchy, R.T. (2002). Melatonin as a chronobiotic/anticancer agent: cellular, biochemical, and molecular mechanisms of action and their implications for circadian-based cancer therapy. Curr. Top. Med. Chem. *2*, 113–132.

Bouchard-Cannon, P., Mendoza-Viveros, L., Yuen, A., Kærn, M., and Cheng, H.Y. (2013). The circadian molecular clock regulates adult hippocampal neurogenesis by controlling the timing of cell-cycle entry and exit. Cell Rep. *5*, 961–973.

Bray, N.L., Pimentel, H., Melsted, P., and Pachter, L. (2016). Near-optimal probabilistic RNA-seq quantification. Nat. Biotechnol. *34*, 525–527.

Brown, E.N., Lydic, R., and Schiff, N.D. (2010). General anesthesia, sleep, and coma. N. Engl. J. Med. *363*, 2638–2650.

Challet, E. (2019). The circadian regulation of food intake. Nat. Rev. Endocrinol. *15*, 393–405.

Codega, P., Silva-Vargas, V., Paul, A., Maldonado-Soto, A.R., Deleo, A.M., Pastrana, E., and Doetsch, F. (2014). Prospective identification and purification of quiescent adult neural stem cells from their in vivo niche. Neuron *82*, 545–559.

Danielson, N.B., Turi, G.F., Ladow, M., Chavlis, S., Petrantonakis, P.C., Poirazi, P., and Losonczy, A. (2017). In vivo imaging of dentate gyrus mossy cells in behaving mice. Neuron *93*, 552–559.e4.

de Faria Poloni, J., Feltes, B.C., and Bonatto, D. (2011). Melatonin as a central molecule connecting neural development and calcium signaling. Funct. Integr. Genomics *11*, 383–388.

Deng, H., Gerencser, A.A., and Jasper, H. (2015). Signal integration by Ca(2+) regulates intestinal stem-cell activity. Nature *528*, 212–217.

Doetsch, F., Petreanu, L., Caille, I., Garcia-Verdugo, J.M., and Alvarez-Buylla, A. (2002). EGF converts transit-amplifying neurogenic precursors in the adult brain into multipotent stem cells. Neuron *36*, 1021–1034.

Dolmetsch, R.E., Lewis, R.S., Goodnow, C.C., and Healy, J.I. (1997). Differential activation of transcription factors induced by Ca2+ response amplitude and duration. Nature *386*, 855–858.

Dolmetsch, R.E., Xu, K., and Lewis, R.S. (1998). Calcium oscillations increase the efficiency and specificity of gene expression. Nature *392*, 933–936.

Dulken, B.W., Leeman, D.S., Boutet, S.C., Hebestreit, K., and Brunet, A. (2017). Single-cell transcriptomic analysis defines heterogeneity and transcriptional dynamics in the adult neural stem cell lineage. Cell Rep. *18*, 777–790.

Fischer, J., Beckervordersandforth, R., Tripathi, P., Steiner-Mezzadri, A., Ninkovic, J., and Götz, M. (2011). Prospective isolation of adult neural stem cells from the mouse subependymal zone. Nat. Protoc. *6*, 1981–1989.

He, L., Si, G., Huang, J., Samuel, A.D.T., and Perrimon, N. (2018). Mechanical regulation of stem-cell differentiation by the stretch-activated Piezo channel. Nature *555*, 103–106.

Hemmings, H.C., Jr., Akabas, M.H., Goldstein, P.A., Trudell, J.R., Orser, B.A., and Harrison, N.L. (2005). Emerging molecular mechanisms of general anesthetic action. Trends Pharmacol. Sci. *26*, 503–510.

Hodeify, R., Yu, F., Courjaret, R., Nader, N., Dib, M., Sun, L., Adap, E., Hubrack, S., and Machaca, K. (2018). Regulation and role of store-operated Ca(2+) entry in cellular proliferation. In Calcium Entry Channels in Non-Excitable Cells, J.A. Kozak and J.W. Putney, Jr., eds. (CRC Press/Taylor & Francis), pp. 215–240.

Horsley, V., Aliprantis, A.O., Polak, L., Glimcher, L.H., and Fuchs, E. (2008). NFATc1 balances quiescence and proliferation of skin stem cells. Cell *132*, 299–310.

Ishii, T., Sato, K., Kakumoto, T., Miura, S., Touhara, K., Takeuchi, S., and Nakata, T. (2015). Light generation of intracellular Ca(2+) signals by a genetically encoded protein BACCS. Nat. Commun. *6*, 8021.

Joppé, S.E., Hamilton, L.K., Cochard, L.M., Levros, L.C., Aumont, A., Barnabé-Heider, F., and Fernandes, K.J. (2015). Bone morphogenetic protein dominantly suppresses epidermal growth factor-induced proliferative expansion of adult forebrain neural precursors. Front. Neurosci. *9*, 407.

Kim, Y., Comte, I., Szabo, G., Hockberger, P., and Szele, F.G. (2009). Adult mouse subventricular zone stem and progenitor cells are sessile and epidermal growth factor receptor negatively regulates neuroblast migration. PLoS ONE *4*, e8122.

Kim, D., Kim, H.J., and Ahn, S. (2018). Anesthetics mechanisms: a review of putative target proteins at the cellular and molecular level. Curr. Drug Targets *19*, 1333–1343.

Labun, K., Montague, T.G., Krause, M., Torres Cleuren, Y.N., Tjeldnes, H., and Valen, E. (2019). CHOPCHOP v3: expanding the CRISPR web toolbox beyond genome editing. Nucleic Acids Res. *47* (W1), W171–W174.

Leeman, D.S., Hebestreit, K., Ruetz, T., Webb, A.E., McKay, A., Pollina, E.A., Dulken, B.W., Zhao, X., Yeo, R.W., Ho, T.T., et al. (2018). Lysosome activation clears aggregates and enhances quiescent neural stem cell activation during aging. Science *359*, 1277–1283.

Lepko, T., Pusch, M., Müller, T., Schulte, D., Ehses, J., Kiebler, M., Hasler, J., Huttner, H.B., Vandenbroucke, R.E., Vandendriessche, C., et al. (2019). Choroid plexus-derived miR-204 regulates the number of quiescent neural stem cells in the adult brain. EMBO J. *38*, e100481.

Lewis, L.D., Piantoni, G., Peterfreund, R.A., Eskandar, E.N., Harrell, P.G., Akeju, O., Aglio, L.S., Cash, S.S., Brown, E.N., Mukamel, E.A., and Purdon, P.L. (2018). A transient cortical state with sleep-like sensory responses precedes emergence from general anesthesia in humans. eLife *7*, 7.

Li, W., Llopis, J., Whitney, M., Zlokarnik, G., and Tsien, R.Y. (1998). Cell-permeant caged InsP3 ester shows that Ca2+ spike frequency can optimize gene expression. Nature *392*, 936–941.

Llorens-Bobadilla, E., Zhao, S., Baser, A., Saiz-Castro, G., Zwadlo, K., and Martin-Villalba, A. (2015). Single-cell transcriptomics reveals a population of dormant neural stem cells that become activated upon brain injury. Cell Stem Cell *17*, 329–340.

Luchsinger, L.L., Strikoudis, A., Danzl, N.M., Bush, E.C., Finlayson, M.O., Satwani, P., Sykes, M., Yazawa, M., and Snoeck, H.W. (2019). Harnessing hematopoietic stem cell low intracellular calcium improves their maintenance in vitro. Cell Stem Cell *25*, 225–240.e7.

Macchi, M.M., and Bruce, J.N. (2004). Human pineal physiology and functional significance of melatonin. Front. Neuroendocrinol. *25*, 177–195.

MacDougall, M.S., Clarke, R., and Merrill, B.J. (2019). Intracellular Ca^{2+} homeostasis and nuclear export mediate exit from naive pluripotency. Cell Stem Cell *25*, 210–224.e6.

Malvaut, S., and Saghatelyan, A. (2016). The role of adult-born neurons in the constantly changing olfactory bulb network. Neural Plast. *2016*, 1614329.

Nakahara, D., Nakamura, M., Iigo, M., and Okamura, H. (2003). Bimodal circadian secretion of melatonin from the pineal gland in a living CBA mouse. Proc. Natl. Acad. Sci. USA *100*, 9584–9589.

Obernier, K., and Alvarez-Buylla, A. (2019). Neural stem cells: origin, heterogeneity and regulation in the adult mammalian brain. Development *146*, dev156059.

Paul, A., Chaker, Z., and Doetsch, F. (2017). Hypothalamic regulation of regionally distinct adult neural stem cells and neurogenesis. Science *356*, 1383–1386.

Pecenin, M.F., Borges-Pereira, L., Levano-Garcia, J., Budu, A., Alves, E., Mikoshiba, K., Thomas, A., and Garcia, C.R.S. (2018). Blocking IP_3 signal transduction pathways inhibits melatonin-induced Ca^{2+} signals and impairs P. falciparum development and proliferation in erythrocytes. Cell Calcium *72*, 81–90.

Petrik, D., Myoga, M.H., Grade, S., Gerkau, N.J., Pusch, M., Rose, C.R., Grothe, B., and Götz, M. (2018). Epithelial sodium channel regulates adult neural stem cell proliferation in a flow-dependent manner. Cell Stem Cell *22*, 865–878.e8.

Pilz, G.A., Bottes, S., Betizeau, M., Jörg, D.J., Carta, S., Simons, B.D., Helmchen, F., and Jessberger, S. (2018). Live imaging of neurogenesis in the adult mouse hippocampus. Science *359*, 658–662.

Plikus, M.V., Vollmers, C., de la Cruz, D., Chaix, A., Ramos, R., Panda, S., and Chuong, C.M. (2013). Local circadian clock gates cell cycle progression of transient amplifying cells during regenerative hair cycling. Proc. Natl. Acad. Sci. USA *110*, E2106–E2115.

Samsa, W.E., Vasanji, A., Midura, R.J., and Kondratov, R.V. (2016). Deficiency of circadian clock protein BMAL1 in mice results in a low bone mass phenotype. Bone *84*, 194–203.

Song, J., Olsen, R.H., Sun, J., Ming, G.L., and Song, H. (2016). Neuronal circuitry mechanisms regulating adult mammalian neurogenesis. Cold Spring Harb. Perspect. Biol. *8*, a018937.

Thestrup, T., Litzlbauer, J., Bartholomäus, I., Mues, M., Russo, L., Dana, H., Kovalchuk, Y., Liang, Y., Kalamakis, G., Laukat, Y., et al. (2014). Optimized ratiometric calcium sensors for functional in vivo imaging of neurons and T lymphocytes. Nat. Methods *11*, 175–182.

Thomas, H.R., Percival, S.M., Yoder, B.K., and Parant, J.M. (2014). High-throughput genome editing and phenotyping facilitated by high resolution melting curve analysis. PLoS ONE *9*, e114632.

Tinhofer, I., Maly, K., Dietl, P., Hochholdinger, F., Mayr, S., Obermeier, A., and Grunicke, H.H. (1996). Differential Ca2+ signaling induced by activation of the epidermal growth factor and nerve growth factor receptors. J. Biol. Chem. *271*, 30505–30509.

Urbán, N., Blomfield, I.M., and Guillemot, F. (2019). Quiescence of adult mammalian neural stem cells: a highly regulated rest. Neuron *104*, 834–848.

Please cite this article in press as: Gengatharan et al., Adult neural stem cell activation in mice is regulated by the day/night cycle and intracellular calcium dynamics, Cell (2021), https://doi.org/10.1016/j.cell.2020.12.026

STAR★METHODS

KEY RESOURCES TABLE

REAGENT or RESOURCE	SOURCE	IDENTIFIER
Antibodies		
Rabbit polyclonal anti-Ki67	Abcam	Cat# ab15580; RRID:AB_443209
Chicken polyclonal anti-GFP	Avès	Cat#GFP-1020; RRID:AB_10000240
Rat monoclonal anti-BrdU	Bio-rad	Cat#MCA2060, RRID:AB_323427
Rabbit polyclonal anti- S100β	Dako	Cat# Z0311, RRID:AB_10013383
Mouse monoclonal anti-Mash1	BD Biosciences	Cat#556604, RRID:AB_396479
Guinea Pig polyclonal anti-Dcx	Millipore	Cat# AB2253, RRID:AB_1586992
Mouse Monoclonal anti-GFP	Life technologies	Cat#A-11120, RRID:AB_221568
Mouse monoclonal anti-**PCNA**	Millipore Sigma	Cat#P8825, RRID:AB_477413
Mouse monoclonal anti- mRFP	BioVision	Cat#3984-100,
Mouse monoclonal anti- GFAP	Millipore	Cat# MAB360, RRID:AB_11212597
Recombinant DNA		
CMV-GCaMP6s	Addgene	Plasmid # 40753
Q13 CMV-geminin-mcherry	this paper	Sequence modified from Sakaue-Sawano et al., 2008
CMV-RFP	Addgene	Plasmid #54764
CMV-GFP	ClonTech	Plasmid # U55763
CMV-Twitch-2B	Addgene	Plasmid # 49531
CMV-mCherry	this paper	Sequences modified from Zhang et al. Nature. 2007
CMV-hBACCS2-IRES-GFP	Addgene	Plasmid # 72891
PU6-BbsI-CBh-Cas9-T2AmCherry	Addgene	Plasmid # 64324
Chemicals		
2 APB	Tocris	Cat# 1224 CAS: 524-95-8
DL-AP5	Tocris	Cat# 0105 CAS: 76326-31-3
HC067047	Tocris	Cat# 4100 CAS: 883031-03-6
SKF 96365	Abcam	Cat# ab120280 CAS: 130495-35-1
Thapsigargin	Tocris	Cat# 1138 CAS: 67526-95-8
Melatonin	Tocris	Cat# 3530 CAS: 73-31-4
Luzindole	Tocris	Cat# 0877 CAS: 117946-91-5
Rhod 2-AM	ThermoFisher Scientific	Cat# R1245MP
Paraformaldehyde	Millipore Sigma	Cat# P6148; CAS: 30525-89-4
BrdU	Millipore Sigma	Cat#B5002-5G; CAS: 59-14-3
Trypsin-EDTA	ThermoFisher Scientific	Cat#15400054
NeuroCult Proliferation Supplement	StemCell Technologies	Cat# 05701

(*Continued on next page*)

Please cite this article in press as: Gengatharan et al., Adult neural stem cell activation in mice is regulated by the day/night cycle and intracellular calcium dynamics, Cell (2021), https://doi.org/10.1016/j.cell.2020.12.026

Continued

REAGENT or RESOURCE	SOURCE	IDENTIFIER
NeuroCult Basal Medium	StemCell Technologies	Cat# 05700
EGF	Sigma-Aldrich	Cat# E4127 CAS: 62229-50-9
bFGF	Sigma-Aldrich	Cat# SRP4038
Heparin	StemCell Technologies	Cat# 07980
Anhydrous ethyl alcohol	Commercial Alcohols	Cat#P016EAAN
Hydrochloric acid (HCl)	Laboratoire Mat	Cat# CR-0166
DiI	ThermoFisher Scientific	Cat# D282
Dimethyl sulfoxide	Millipore Sigma	Cat# D2650 CAS: 67-68-5
Sodium Chloride (NaCl)	Fisher Scientific	Cat# S271-3; CAS: 7647-14-5
Potassium chloride (KCl)	Millipore Sigma	Cat#P9541; CAS:7447-40-7
Magnesium chloride ($MgCl_26H_20$)	Millipore Sigma	Cat# M8266; CAS: 7786-30-3
Sodium bicarbonate ($NaHC0_3$)	Millipore Sigma	Cat# S5761 CAS: 144-55-8
Sodium dihydrogen phosphate monohydrate (NaH_2P0_4 H_20)	VWR	Cat# CA71008-768; CAS: 10049-21-5
Dextrose (D-Glucose)	Fisher Scientific	Cat# D16-3 CAS: 50-99-7
Calcium chloride dehydrate ($CaCl_2$ $2H_20$)	Millipore Sigma	Cat# C3881; CAS: 10035-04-8
Sucrose	Fisher Scientific	Cat#S5-3; CAS: 57-50-1
Trisodium citrate dihydrate	Millipore Sigma	Cat# S1804 CAS: 6132-04-3
Triton X-100	Amresco	Cat#M143
C&B Metabond Quick Base	Parkell	Cat# S398
AmalgamBond/MetaBond Catalyst 7ml Bt	Parkell	Cat# S371
C&B Metabond Powder Clear 3g Bt	Parkell	Cat# S399
Critical commercial assays		
Maxi Prep	QIAGEN	Cat# 12362
DNeasy Blood & Tissue Kit	QIAGEN	Cat# 69504
LightCycler 480 High Resolution Melting Master	Roche	Cat# 04909631001
RNAscope Multiplex Fluorescent Reagent Kit	Advanced Cell Diagnostics	Cat# 320850
Experimental models: organisms/strains		
Mouse: CD1	Charles Rivers	Strain code: 022
Mouse: GFAP-GFP	Jackson	Strain code: 003257 FVB/N-Tg(GFAPGFP)14Mes/J
Oligonucleotides, gRNA sequences and RNAscope probes		
gRNA sequences against Itpr2 and LacZ	This paper	Sequences provided below in STAR methods
RNAscope probes against GFP	Advanced Cell Diagnostics	400281-C1
RNAscope probes against mCherry	Advanced Cell Diagnostics	431201-C2
RNAscope probes against MTR1a	Advanced Cell Diagnostics	403601-C3
RNAscope probes against MTR1b	Advanced Cell Diagnostics	502451-C3
HRM PCR primers	This paper	Sequences provided below in STAR methods

(*Continued on next page*)

Please cite this article in press as: Gengatharan et al., Adult neural stem cell activation in mice is regulated by the day/night cycle and intracellular calcium dynamics, Cell (2021), https://doi.org/10.1016/j.cell.2020.12.026

Continued

REAGENT or RESOURCE	SOURCE	IDENTIFIER
Software and algorithms		
MATLAB 2016a	Mathworks	https://www.mathworks.com/
MATLAB scripts for Ca^{2+} imaging analysis	This paper	https://github.com/SagLab-CERVO/Calcium_analysis_in_NSC
ImageJ	NIH	https://imagej.net/Welcome
Origin 2016	OriginLab Corporation	https://www.originlab.com/
Statistica 6.1	Stat Soft	N/A
Primer-Blast software	NCBI	https://login.acces.bibl.ulaval.ca/login?qurl=https://www.ncbi.nlm.nih.gov%2ftools%2fprimer-blast%2f
ChopChop online software	Labun et al., 2019	https://chopchop.cbu.uib.no/
LightCycler 480 SW1.5.1 software	Roche	04994884001
Others		
PCR 96 well plates	Bio-Rad	1199933
Snap-in Imaging Cannula, Model L-VP Prism orientation 1 Depth range: 2.9mm – 5.9mm	Doric Lenses	Cat# SICL_V_500_80_P_1
Snap-in Imaging Cannula, Model L-V Depth range: 2.87mm – 5.96mm	Doric Lenses	Cat# SICL_V_500_80
Dual Fiber-optic Cannulas	Doric Lenses	Cat#DFC-200/250-0.66-2.7mm-GS0.7-MA45, 200 μm diameter fiber
Basic Fluorescence Microscopy System - Deep Brain	Doric Lenses	Cat#BFMS-L_UFGJ_1000_900_458_D
2-color Fluorescence Microscopy System - Deep Brain	Doric Lenses	Cat#2CMS-LD_UFGJ_1000_900_458/561
Optogenetically Synchronized Fluorescence Microscopy System - Deep Brain	Doric Lenses	Cat#OSMS-L_UFGJ_1000_900_445/616_D

RESOURCE AVAILABILITY

Lead contact

Further information and requests for resources and reagents should be directed to and will be fulfilled by the Lead Contact, Armen Saghatelyan (armen.saghatelyan@fmed.ulaval.ca).

Material availability

This study did not generate new unique reagents.

Data and code availability

The code for analysis of Ca^{2+} activity in NSCs is available at https://github.com/SagLab-CERVO/Calcium_analysis_in_NSC. All FastQ files are available at GEO. Accession number: GSE161276.

EXPERIMENTAL MODEL AND SUBJECT DETAILS

The experiments were performed using two- to six-month-old CD1 (Charles River) and glial fibrillary acidic protein (GFAP)-GFP (The Jackson Laboratory) mice of both sexes, which were electroporated on postnatal days 0-1 (P0-P1). All experiments were approved by the Université Laval animal protection committee. The mice were housed one to five per cage. It should be noted that while mice are nocturnal animals, in our experiments we did not assess their locomotor activity during the day and night. They were kept on a 12-h light/dark cycle at a constant temperature (22°C) with food and water *ad libitum*.

METHOD DETAILS

Electroporation

For the electroporation of plasmids, P0-P1 CD-1 or GFAP-GFP pups were anesthetized by hypothermia and were placed on the stereotactic frame. The plasmids (1 μL, 3-6 μg/μL total, except for GFAP-GCaMP6s and GFAP-Twitch-2B) were injected in the lateral ventricle using the following coordinates (with respect to the lambda): anterior-posterior (AP) 1.8 mm, medio-lateral (ML) 0.8 mm,

and dorso-ventral (DV) 1.6 mm. For GFAP-GCaMP6s and GFAP-Twitch2B not more than 1 μg/μL of 1 μL of solution was used to avoid buffering the intracellular Ca^{2+} with these Ca^{2+} indicators. We used the following plasmids: CMV-GCaMP6s (#40753, Addgene), kindly provided by Dr. Kim & GENIE Project, Janelia Research Campus; CMV-geminin$_{1-110}$-mCherry, kindly provided by Dr. Miyawaki, RIKEN; CMV-RFP (#54764, Addgene), kindly provided by Drs. Campbell, Davidson, and Tsien; CMV-GFP (#U55763, Clontech), CMV-Twitch-2B (#49531, Addgene), kindly provided by Dr. Griesbeck, Max Planck Institute; and CMV-hBACCS2-IRES-GFP (#72891, Addgene), kindly provided by Dr. Nakata, Tokyo Medical University. CMV-mCherry was generated by PCR amplification of the cDNA encoding mCherry from pLenti-CaMKII-hChR2-mCherry-WPRE (a gift from Dr. Deisseroth, Stanford University) with primers 5′-GCGCTACCG GTCGCCACCATGGTGAGCAAGGGCGAGGAGGATAACA-3′ and 5′-CTTGTACAGCTCGTCCATGCCGC-3′. The PCR product was then digested with AgeI–BsrGI and was inserted into the AgeI–BsrGI sites of U55763 vector (Clontech). GCaMP6s, Twitch-2B, hBACCS2-IRES-GFP, and GFP were sub-cloned under the GFAP promoter while mCherry was subcloned under the prominin (P2) promoter (Beckervordersandforth et al., 2010). The plasmid solution was supplemented with 1% Fast-Green to visualize the injection and ensure that the ventricle was filled with plasmid solution. Immediately after the injection, an electric field (five 50-ms 100-mV pulses at 950-ms intervals) was applied using an electrode positioned on the surface of the bones and coated with conductive gel. The pups were used 2-4 months post-electroporation. In experiments with gRNAs, we also analyzed mice 10 days post-electroporation. We used gRNAs for *Itpr2* as well as for LacZ, as a control. We used two different gRNAs for *Itpr2* and electroporated these plasmids together. The gRNAs were cloned in the BbsI site of the PU6-BbsI-CBh-Cas9-T2AmCherry plasmid (#64324, Addgene) kindly provided by Dr. Kuehn, Berlin Institute of Health) in which CBh was replaced by the P2 promoter.

Gradient index (GRIN) lens implantation and *in vivo* imaging in freely behaving mice

Adult 2- to 3-month-old CD1 mice electroporated with different plasmids at P0-P1 were anesthetized with isoflurane (2%–3%) and were placed on the stereotactic frame. The temperature of the animals was maintained at 37°C throughout the procedure using an infrared blanket (Kent Scientific). An incision was made in the skin, a hole centered over the subventricular zone (SVZ) or lateral ventricle (LV) was drilled, and a cannula composed of a GRIN lens (0.5 mm in diameter and 3-5 mm in length) and an adjustment ring (Doric Lenses) was slowly lowered into the SVZ or LV to detect fluorescently labeled cells or overall changes in fluorescence. Metabond cement (Parkell Inc.) was used to fix the cannulas on the skull, and the skin was sutured. We used two different cannulas. In most cases we used a "side-view" cannula composed of a GRIN lens with a 45° prism glued to it. This configuration made it possible to insert the cannula into the LV and to detect fluorescently labeled cells during implantation. We also used a cannula with a flat GRIN lens implanted just above the SVZ (Figure S1), which was determined by changes in the overall background fluorescence during implantation. Mini-endoscopic imaging started 10-14 days after the insertion of the side-view GRIN lens and 2-3 weeks after the implantation of the flat GRIN lens. To ensure that the positioning of the flat GRIN lens did not affect proliferation in the SVZ at the time of *in vivo* imaging, we removed the GRIN lens from a few mice 2-3 weeks post-implantation and immunolabelled for Ki67. No changes in the proliferation of NSCs were detected (Figure S1). The cannulas were connected either to a one-color or a two-color mini-endoscope (Doric Lenses). The same cells could be imaged for up to 2-3 months. Imaging sessions consisted of 2-3 days of continuous imaging, with one image acquired every 15 min. For the GFAP-GCaMP6s experiments, the mice were imaged for 1 h with 1 image acquired every 30 s. The images were recorded for the XY positions and were corrected for xy drift using the StackReg ImageJ plugin, as needed. The two-color mini-endoscope allowed us to image cells labeled with two different fluorophores and driven by two different promoters. For these experiments, the mice were electroporated at P0-P1 with a combination of either CMV-RFP and P2-GFP or GFAP-GCaMP6s and CMV-geminin-mCherry. For the cell division experiments using the CMV-RFP and P2-GFP combination, the ubiquitous CMV promoter (instead of GFAP) made it possible to reliably detect fluorescent cells after cell division and avoid situations in which divided cells were not detected due to the lack of GFAP and P2 promoter activity in the daughter cells. For one-color mini-endoscopic imaging of GFP or GCaMP6, we used 458/35 and 525/40 excitation and emission filters, respectively, with a 300-ms exposure time. For two-color mini-endoscopic imaging, we used LED and YAG illumination sources (Doric Lenses) with 430-477 nm and 558-564 nm excitation filters for GCaMP6s (or GFP) and mCherry imaging, respectively, and 520/35 and 615/45 emission filters, respectively, with a 300-ms exposure time.

In vivo optogenetic stimulation

For *in vivo* optogenetic stimulations, adult CD1 mice that had been electroporated at P0-P1 with GFAP-hBACCS2-GFP (or GFAP-GFP as a control) and Itpr2 gRNA-P2-Cas9-T2A-mCherry (or P2-mCherry) were anesthetized with isoflurane (2%–3%) and were placed on the stereotactic frame. The surgery was performed as described above, and two optogenetic fibers (DFC-200/250-0.66-2.7mm-GS0.7-MA45, 200 μm diameter fiber; Doric Lenses), with a 0.7-mm pitch between fibers, were slowly lowered into the LV at the following coordinates: AP 0.5 mm; ML 0.4-1.1 mm; and DV 2.2 mm. The tips of both fibers had a mirror angle of 45°, which made it possible to direct the light to the lateral wall of the LV. The 0.7-mm pitch made it possible to cover the entire medio-lateral portion of the SVZ. After a 2- week recovery period, the mice were connected to a 488-LED illumination source, and 4.1-mW/mm^2 60 s pulses were randomly delivered five times over a period of 1 h for 3 days. The length of the stimuli was based on the properties of hBACCS2, which has a peak Ca^{2+} response at 60 s (Ishii et al., 2015). Since *Itpr2* gene editing caused a 2-fold decrease in the frequency of Ca^{2+} events in qNSCs (Figure 6), we optogenetically stimulated NSCs to compensate for the reduced frequency. After the 3-day stimulation protocol, the mice were perfused and 40-μm-thick brain slices were immunolabelled

Please cite this article in press as: Gengatharan et al., Adult neural stem cell activation in mice is regulated by the day/night cycle and intracellular calcium dynamics, Cell (2021), https://doi.org/10.1016/j.cell.2020.12.026

for Ki67. The same stimulation parameters were used for the experiments with 250-lux constant light condition. Proliferative NSCs were counted in the entire medio-lateral portion of the dorsal SVZ.

To validate that optogenetic stimulation covers the entire medio-lateral portion of the SVZ, we modeled the light diffusion in the brain based on the illumination power, the angle of the fibers, and the pitch between two fibers (Figure S5). The modeling was performed using Zemax software. We used a non-sequential mode and launch 1 M rays for each LED. The simulation models two LED sources with Lambertian angular distribution, followed by two short length of optical fiber (10 mm) using 2 cylinder object with core and cladding. The small absorbing volume was added to remove ray that escape from optical fiber and increase computation speed. Optical fiber is immerged in a seawater media. Detector is a volume detector with Voxel size of 0.01 mm in x, y and z. Power value of a pixel in the Volume Detector (Watt) correspond 0.0001 mm^2 area, then should be multiplied by 1E4 to get value in W/mm^2 (or 1E7 for mW/mm^2). Another detector rectangle is placed at output of one fiber to adjust output power to 0.125 mW. The resulting image (Figure S5) is a linear scale plot with maximum intensity corresponding to 4 mW/mm^2.

In vivo luzindole and melatonin treatments and constant light/darkness conditions

For the constant light or constant darkness experiments, adult CD1 mice that had been electroporated at P1-P2 with the GFAP-GFP and P2-mCherry plasmids were transferred to a room either with constant 250-lux light illumination or with constant darkness for 3 or 7 days. The control mice were kept on a normal 12 h/12 h light/dark cycle. For the luzindole experiments, adult CD1 mice electroporated at P1-P2 with the GFAP-GFP and P2-mCherry plasmids were injected intraperitoneally with luzindole (10 mg/kg in 2% DMSO) twice a day for 7 days. As melatonin secretion is bimodal, with a peak at 7 p.m. and another peak at midnight (Nakahara et al., 2003), we injected the mice at 6 p.m. and 11 p.m. The mice in the control group received injections of 2% DMSO. We also injected luzindole during a day, when melatonin level is lower. In these experiments, we injected the mice with luzindole (10 mg/kg in 2% DMSO) twice a day for 7 days, at 9 a.m. and 2 p.m. To increase melatonin levels during the daytime, we injected melatonin (8 mg/kg) at 9 a.m. and 2 p.m. for 7 days. Following the 7-d period, the mice were perfused, and 40-μm-thick brain slices were immunolabelled for Ki67 to assess the number of proliferative GFP+/mCherry+ NSCs.

BrdU label-retaining protocol

In order to distinguish between astrocytes and NSCs in adult GFAP-GFP mice, a DNA replication marker (BrdU) was given in the drinking water (1 mg/mL in 0.3% sucrose) for 2 weeks followed by a 3-week ''chase'' period during which the mice received only water.

Transcriptome analysis of prospectively isolated qNSCs and aNSCs

FACS of different populations from the adult mouse brain SVZ was performed as previously described (Beckervordersandforth et al., 2010; Fischer et al., 2011). The following cell types from hGFAP-GFP animals were sorted: qNSC (hGFAP-GFP+, CD133+, EGFR-; dataset already used in (Lepko et al., 2019)) and aNSCs (hGFAP-GFP+, CD133+, EGFR+). FACS-purified cells were collected and were homogenized in RLT buffer (QIAGEN). Total RNA was extracted using the miRNeasy Mini Kit (QIAGEN) according to the manufacturer's instructions, including the step for the removal of genomic DNA. An Agilent 2100 Bioanalyzer was used to assess RNA quality.

To prepare libraries for RNA-sequencing, cDNA was synthesized from 300 pg of total RNA using a SMART-Seq v4 Ultra Low Input RNA Kit for Sequencing (Clontech), according to the manufacturer's instructions. Prior to generating the final library for Illumina sequencing, the Covaris AFA system was used to perform cDNA shearing, resulting in 200-500-bp-long cDNA fragments. The quality and concentration of the sheared cDNA was assessed on an Agilent 2100 Bioanalyzer before preparing the library using MicroPlex Library Preparation Kit v2 (Diagenode). Final libraries were evaluated and quantified using an Agilent 2100 Bioanalyzer, and the concentrations were measured using a Quant-iT PicoGreen dsDNA Assay Kit (ThermoFisher Scientific) before sequencing. The uniquely barcoded libraries were multiplexed onto one lane, and 100-bp paired-end deep sequencing was carried out on a HiSeq 4000 (Illumina) that generated ~30 million reads per sample. FastQ files were deposited at NCBI Central (accession number pending). Kallisto pipeline (Bray et al., 2016) was used to quantify the expression of transcripts that are expressed as transcripts per million reads (tpm). To verify the sorting, we analyzed the expression of highly expressed genes in different cellular populations defined using an independent scRNaseq based approach (Llorens-Bobadilla et al., 2015).

CRISPR target site selection and assembly

The gRNAs were designed and selected using ChopChop online software (Labun et al., 2019). We used two different gRNAs to target each gene in order to increase the efficiency of the CRISPR editing. The following gRNA sequences were used:

	gRNA sequences (5′ −3′)
Itpr2-gRNA1	CCTCTGGGTGCACCACACAA
Itpr2-gRNA2	ACACGATGTCCCCAATGTAG
Control, LacZ-gRNA	TGCGAATACGCCCACGCGAT

The efficiency of the gRNAs was verified by high-resolution melting curve PCR (Thomas et al., 2014) on primary cultures of adult NPCs transfected with above-mentioned plasmids under a CMV promoter. Briefly, the thin layer of SVZ bordering the lateral ventricle, excluding the striatal parenchyma and corpus callosum, was dissected from the SVZ of 8- to 12-week-old C57BL/6 mice. The tissue was minced and was digested in a 0.05% trypsin-EDTA solution, following which an equal volume of soybean trypsin inhibitor was added. After trituration, the resulting single cell suspension was cultured in NeuroCult Basal Medium with NeuroCult Proliferation Supplement (StemCell Technologies). EGF and bFGF (10 ng/mL each; Sigma-Aldrich), and heparin (2 μg/mL; StemCell Technologies) was added to the culture medium.

Genomic DNA was isolated using DNeasy Blood & Tissue kits (QIAGEN) according to the manufacturer's protocol. Primers were designed using Primer-Blast software (https://www.ncbi.nlm.nih.gov/tools/primer-blast/).

The PCR reactions were performed with 5 μL of LightCycler® 480 High Resolution Melting Master (Roche), 0.5 μL of each primer (10 μM), 1.2 μL of $MgCl_2$ (25 mM), and 2 μL of genomic DNA and was completed with water to 10 μL. The PCR was performed in a LightCycler 480 (Roche) using 96-well plates (Bio-Rad). The amplification started with an initial 5-min denaturation step at 95°C, followed by 48 cycles at 95°C for 10 s, 60°C for 30 s, and 72°C for 25 s. Melting curves were generated over a 65-95 °C range in 0.2°C increments and were analyzed using LightCycler 480 SW1.5.1 software. The following primers were used:

	HRM Primers (5′-3′)
Itpr2-gRNA1-Fw	GTGGCTTATGAATGTGGTGATG
Itpr2-gRNA1-Rs	CTGAACTTCTTGGGTGGGTT
Itpr2-gRNA2-Fw	GAGCTCACCCTTGCGTGC
Itpr2-gRNA2-Rs	TGAAGCCATTGACCGAGCCC

Immunostaining

The animals were deeply anesthetized with sodium pentobarbital (12 mg/mL; 0.1 mL per 10 g of body weight) and were perfused intracardially with 0.9% NaCl followed by 4% paraformaldehyde (PFA). The brains were collected and were kept overnight in 4% PFA. Sagittal slices (40 μm) were cut using a vibratome (Leica). The brain slices were incubated with the following primary antibodies: mouse (1:500, Life technologies) or chicken anti-GFP (1:500, Aves), rabbit anti-Ki67 (1:500, Abcam), mouse anti-PCNA (1:500, Sigma), mouse anti-GFAP (1:500, Sigma), mouse anti-Mash1 (1:500, BD Bioscience), guinea pig anti-Dcx (1:500, Sigma), rabbit anti-s100β (1:500, Agilent Dako), rat anti-BrdU (1:500, Bio-Rad), and mouse anti-RFP (1:500, BioVision). The antibodies were diluted in 0.5% Triton X-100 and 4% milk prepared in PBS. The brain slices were incubated overnight at 4°C. For PCNA immunolabeling, an antigen retrieval protocol was applied by incubating the sections in Na-citrate solution (pH 9) for 15 min at 80°C. For BrdU immunolabeling, the brain slices were treated with 2 N HCl for 40 min at 37°C to denature the DNA. The corresponding secondary antibodies were used and were applied for 3 h at RT. For proliferation analysis with PCNA, Ki67 and BrdU, the daughter cell doublets were excluded from analysis. For experiments with Twitch2B, adult CD1 mice electroporated with GFAP-Twitch2B at P0-P1 were perfused 8 weeks later, and 40-μm-thick brain slices were immunostained with anti-Ki67. Images were acquired using the CFP excitation wavelength (405 nm), and the fluorescence signals were collected at the CFP and YFP emission wavelengths. The fluorescence signals from the region of interest were calculated as a ratio of YFP to CFP emissions. Fluorescence images were acquired using a confocal microscope (FV 1000; Olympus) with 60x (UPlanSApoN 60x/NA 1.42; Olympus) and 40x (UPlanSApoN 40x/NA 0.90; Olympus) oil and air immersion objectives, respectively.

Time-lapse Ca^{2+} imaging in acute brain slices

Six to 10 weeks post-electroporation, the mice were sacrificed, and acute slices were prepared as described previously (Bakhshetyan and Saghatelyan, 2015). Briefly, the mice were anesthetized with ketamine (100 mg/kg) and xylazine (10 mg/kg) and were perfused transcardially with modified oxygenated artificial cerebrospinal fluid (ACSF) containing (in mM): 210.3 sucrose, 3 KCl, 2 $CaCl_2.2H_2O$, 1.3 $MgCl_2.6H_2O$, 26 $NaHCO_3$, 1.25 $NaH_2PO_4.H_2O$, and 20 glucose. The brains were then quickly removed and 250-μm-thick slices were cut using a vibratome (HM 650V; ThermoFisher Scientific). The slices were kept at 37°C in ACSF containing (in mM): 125 NaCl, 3 KCl, 2 $CaCl_2.2H_2O$, 1.3 $MgCl_2.6H_2O$, 26 $NaHCO_3$, 1.25 $NaH_2PO_4.H_2O$, and 20 glucose under oxygenation for no more than 6-8 h. The acute slices were transferred to the imaging chamber and were continuously superfused with ACSF. Ca^{2+} imaging was performed at 31-33°C using a BX61WI (Olympus) upright microscope equipped with motorized *z* drive, a 40X water immersion objective (NA = 0.8), a CCD camera (CoolSnap HQ), and mercury arc or Xenon illumination lamps. GCaMP6s and Rhod-2 were imaged using 482/35 nm and 562/40 nm excitation filters, and emissions were collected using 536/40 nm and 593/40 nm filters, respectively. The imaging was performed every 30 s for 1-2 h with multiple z stacks (5-9 stacks at 3-μm intervals), except for luzindole experiments when imaging was performed every 10 s for 20-25 min. For pharmacological experiments, the same cells were imaged under baseline conditions for 40-60 min followed by imaging in the presence of different pharmacological compounds for another 40-60 min. For luzindole experiments, we performed imaging only for 20-25 min (10 min at baseline followed by 10-15 min in the presence of luzindole, one acquisition every 10 s) to minimize potential melatonin washout in the acute brain slices by the 1-2 mL/min flow

Please cite this article in press as: Gengatharan et al., Adult neural stem cell activation in mice is regulated by the day/night cycle and intracellular calcium dynamics, Cell (2021), https://doi.org/10.1016/j.cell.2020.12.026

rate of ACSF. The following reagents were used: 2APB (100 μM) to block IP3-sensitive intracellular stores, thapsigargin (3 μM) to inhibit SERCA, luzindole (15 μM) to inhibit melatonin receptors, AP5 (50 μM) to block NMDA receptors, SKF 96365 hydrochloride (25 μM) to block TrpC channels, HC 067047 (10 μM) to block TrpV4 channels and EGF (0.1μg/mL) to increase NSC and progenitor proliferation. For Rhod2-AM experiments in GFAP-hBaccs2 electroporated cells, the slices derived from adult mice electroporated with GFAP-hBaccs2 at P0-P1 were incubated with Rhod2-AM (0.5 μM) for 35-40 min. Baseline fluorescence intensity of Rhod2 was assessed exclusively in hBaccs2+ cells before and after 60 s optogenetic stimulation at 490 nm.

Ca^{2+} imaging analysis

Ca^{2+} responses were analyzed using a custom-written script in MATLAB (MathWorks Inc., USA). The images were recorded for the XY positions and were corrected for xy drift using the StackReg ImageJ plugin, as needed. Regions of interest (ROI) were manually drawn around the soma of each cell to extract the GCaMP6s or Rhod2 fluorescence signal. Ca^{2+} activity in the processes was not analyzed. Ca^{2+} activity was calculated as relative changes in the percentage of $\Delta F/F = (F\text{-}F_{back})/F_{back}$, where F is the GCaMP6 intensity in the ROI and F_{back} is the background signal. To analyze spontaneous Ca^{2+} activity in NSCs we used a multiple threshold algorithm (Danielson et al., 2017). Briefly, we first calculated the mean standard deviation (SD) of each Ca^{2+} trace, and all peaks with an amplitude greater than 2 times the SD were measured. These peaks were then removed from the Ca^{2+} traces, and the mean SD of the Ca^{2+} trace was re-calculated to depict events greater than 2 times the new SD. This procedure was repeated another time and allowed us to depict all Ca^{2+} events regardless of their amplitudes. Three different thresholds for the detection of Ca^{2+} events are shown in **Figures** by dashed lines. Several thresholds (1xSD, 1.5xSD, 2xSD, 2.5xSD) were empirically tested by visually inspecting Ca^{2+} activity.

Post hoc identification of imaged cells

For the post hoc identification of cells imaged in the acute brain slices, 250-μm-thick slices were fixed in 4% PFA overnight and were pre-permeabilized with methanol and acetone (30 min each at –30°C) prior to immunostaining. The brain slices were incubated with anti-GFP, anti-PCNA, and anti-s100β primary antibodies for CD1 mice electroporated with GCaMP6s plasmid and with anti-Ki67, anti-GFP, and anti-BrdU primary antibodies for GFAP-GFP mice injected with the Rhod2-AM organic Ca^{2+} indicator. Rhod2-AM (1 μL of a 1 mM solution in DMSO) was injected into the LV of adult GFAP-GFP mice 1 h prior to the preparation of the acute brain slices at the following coordinates: AP 0.4 mm; ML 0.9 mm, and DV 1.9 and 2.4 mm. The corresponding secondary antibodies were used. Because of the sparse labeling of GFAP-GCaMP6s cells, approximately 80% of the imaged cells were retrieved using a post hoc identification analysis. For the Rhod2-AM experiments, the retrieval rate was lower (approximately 40%) because of the dense labeling of GFAP-GFP and Rhod2-AM. To improve retrieval, a pipette dipped in a 1 mM DiI solution was lowered into the acute slice after the Ca^{2+} imaging and before fixation. Imaged cells that were not retrieved by the post hoc identification analysis were discarded.

RNAscope *in situ* hybridization

For the *in situ* hybridization of MTR1a, MTR1b, GFP, and mCherry, we used RNAscope Multiplex Fluorescent Reagent kits (Advanced Cell Diagnostics) according to the manufacturer's protocol. *In situ* hybridization was performed on 15-μm-thick fresh frozen brain slices derived from CD1 mice electroporated with GFAP-GFP and P2-mCherry at P0-P1. The frozen brain slices were mounted on slides and were dried for 1 h at –20 °C. They were then incubated in cold 4% PFA for 15 min and were sequentially dehydrated in 50%, 70%, and 100% ethanol solutions for 5 min each at RT. The slides were treated with Protease IV for 30 min at RT for antigen retrieval. The probes were diluted (1:50) and were applied to the slides for 2 h at 40°C. The slides were then incubated with a series of preamplifier and amplifier reagents at 40°C (AMP1 for 30 min, AMP2 for 15 min, AMP3 for 30 min, and AMP4 Alt A for 15 min) according to the manufacturer's protocol. Images were acquired using an inverted Zeiss microscope (LSM 700, AxioObserver) with a 20X air immersion objective (NA: 0.9) or a 63X oil immersion objective (NA: 1.4).

QUANTIFICATION AND STATISTICAL ANALYSIS

Data are expressed as means ± SEM. The individual values of all experiments are also shown in the corresponding figures. The investigator was blinded to the experimental conditions for the analysis of the percentage of proliferating NSCs after the electroporation of the gRNAs. Ca^{2+} activity was determined prior to the post hoc identification of imaged cells and, consequently, the investigator was unaware of whether it reflected the activity of astrocytes, qNSCs, or aNSCs. Statistical significance was determined using an unpaired two-sided Student's t test, Mann-Whitney *U* test or one-way ANOVA followed by LSD-Fisher post hoc test, using Statistica software. A paired Student's t test was used for the pharmacological experiments where the same cells were imaged under baseline conditions and following the addition of the pharmacological compound. Equality of variance for the unpaired t test was verified using the F-test. The exact values of *n* and its representation (cells, animals) for all experiments are indicated in Tables S1 and S2. The levels of significance were * $p < 0.05$, ** $p < 0.01$, and *** $p < 0.001$.

CellPress

Supplemental Figures

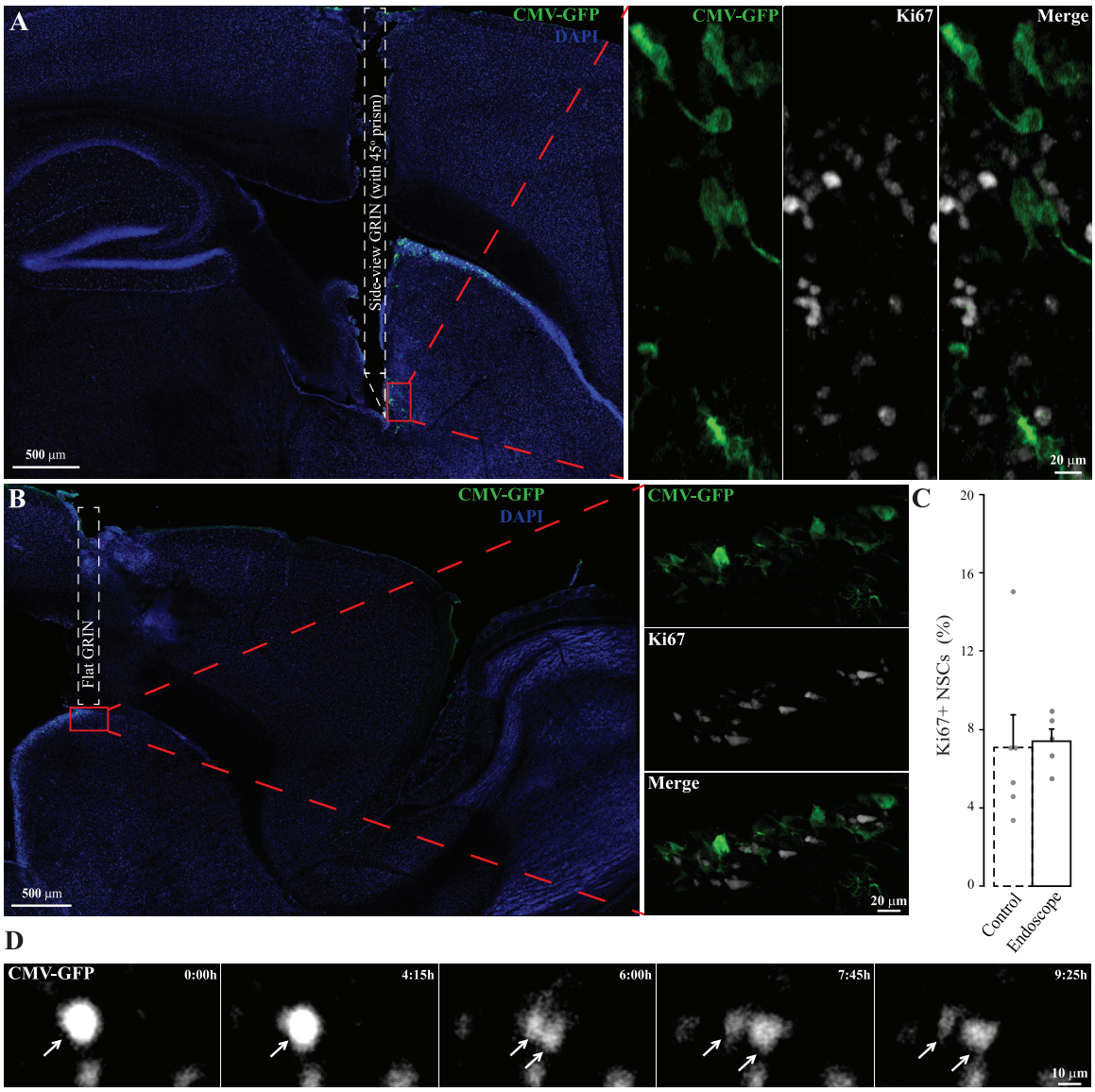

Figure S1. Placement of different types of GRIN lenses used for the *in vivo* imaging and proliferation analyses of NSCs, related to Figure 1 and STAR methods

(A and B) Sagittal brain sections showing the placement of the side-view (A) and flat (B) GRIN lenses in the LV and above the SVZ, respectively. The brain sections were counterstained with DAPI. The placement of the GRIN lenses is indicated by dashed white rectangles. (C) The analysis of proliferative Ki67+ NSCs after the removal of a GRIN lens. The GRIN lens was removed 2-3 weeks after installation, which corresponded to the time when the *in vivo* imaging was started. For comparison purposes, the percentage of proliferative NSCs observed in control condition (without GRIN installation; Figure 1D) is plotted (dashed bar). (D) Snapshot images showing NSC division in the SVZ of freely behaving mice. NSCs were labeled by the electroporation of the CMV-GFP plasmid at P0-P1. The arrows indicate an NSC undergoing cell division. Note the reduced fluorescent intensity in the daughter cells, which is consistent with the dilution of the plasmid. See also Videos S2, S3, and S4.

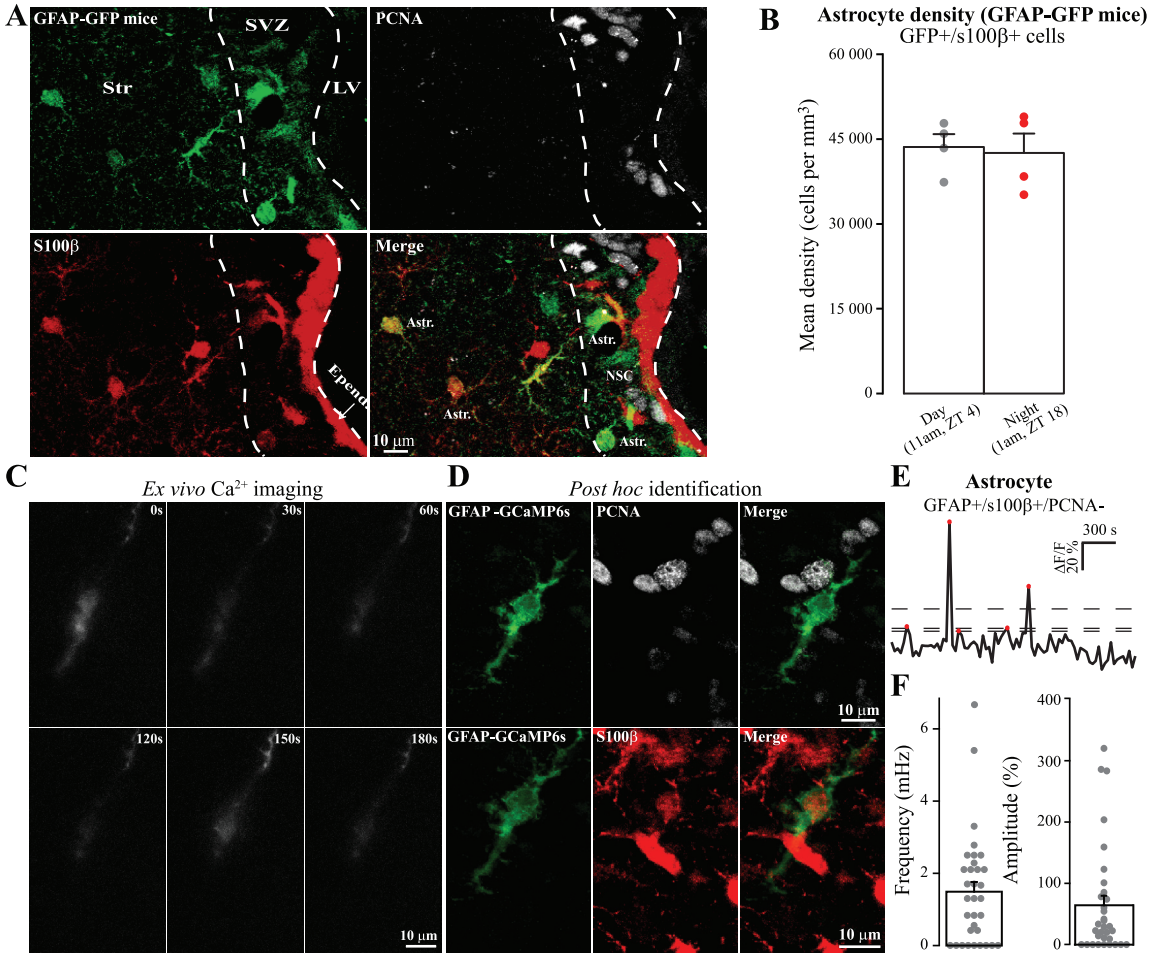

Figure S2. Density of niche astrocytes in the SVZ during the day/night cycle and their Ca^{2+} activity, related to Figures 2 and 3

(A) Confocal images showing s100β and PCNA immunolabeling in GFAP-GFP mice. Note that s100β strongly labels ependymal cells and mature astrocytes in the SVZ and striatum (str), whereas GFAP-GFP depicts astrocytes and stem cells. (B) Quantification of the density of niche astrocytes (GFAP+/s100β+) in the SVZ depending on the day/night cycle. Mice were perfused either during the day (11 a.m.; ZT 4) or night (1 a.m.; ZT 18). (C) Example of Ca^{2+} activity in GFAP-GCaMP6s cells in acute brain slices 2-3 months post-electroporation. (D) *Post hoc* identification of imaged cell using PCNA and s100β immunolabeling. Note that the imaged GFAP-GCaMP6s cell was s100β+/PCNA- and was thus defined as a niche astrocyte. (E and F) Example of a Ca^{2+} activity trace and quantification of the frequency and amplitude of Ca^{2+} events. Dashed lines represent three SD thresholds used for the detection of Ca^{2+} events.

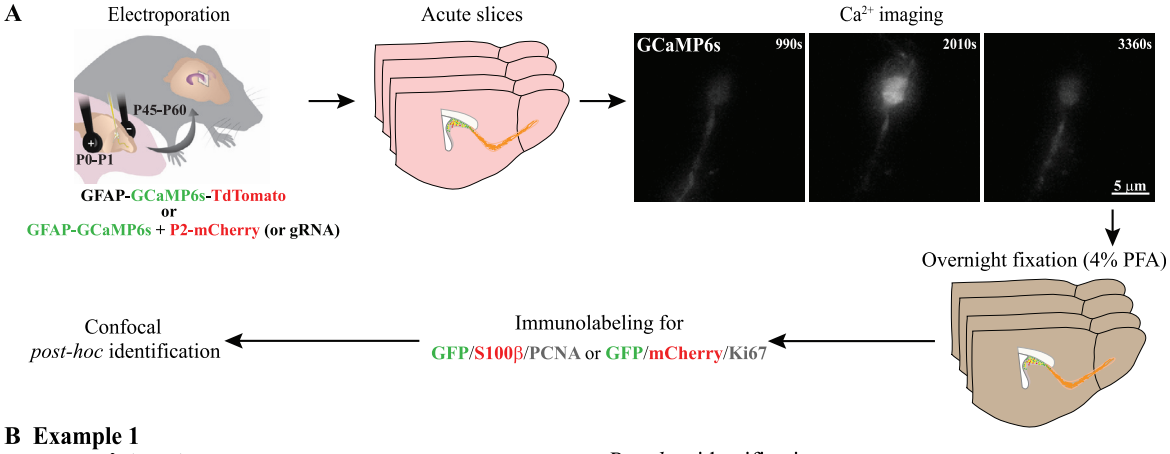

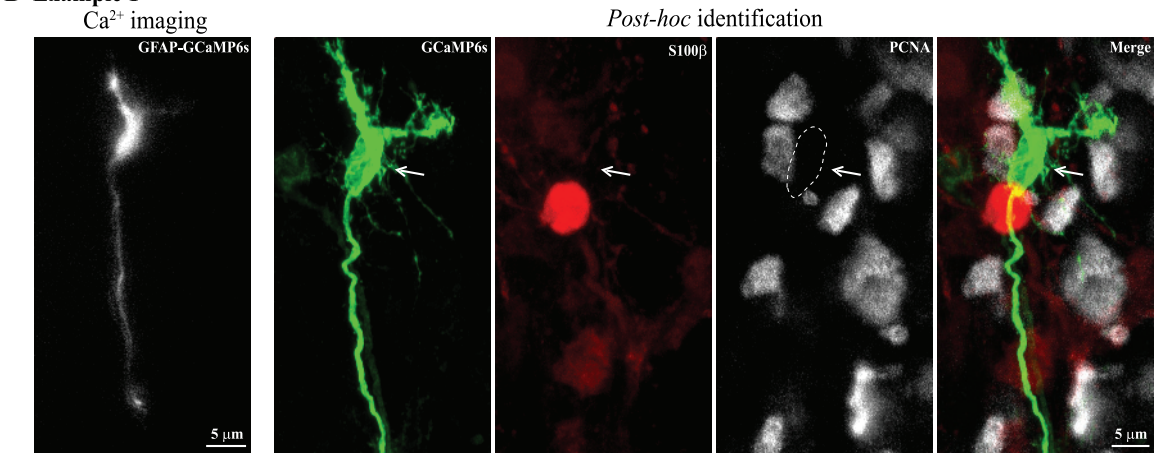

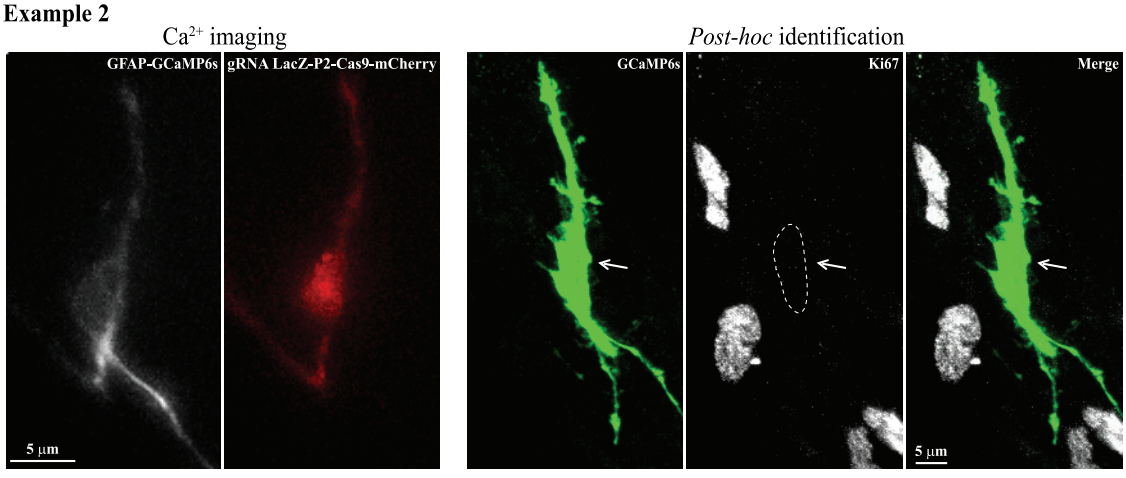

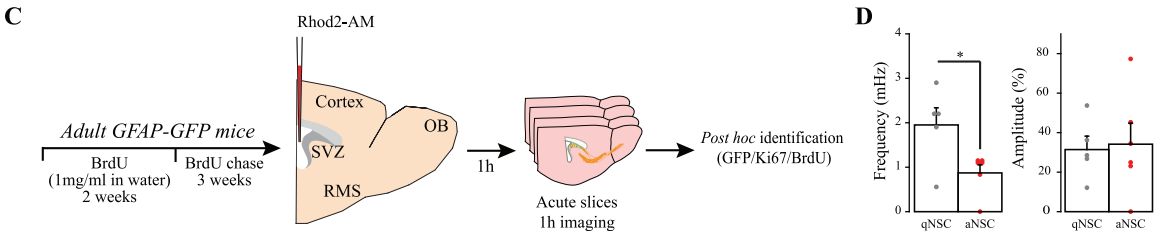

(legend on next page)

Figure S3. Methodological framework for the post hoc identification of NSCs used for Ca^{2+} imaging with genetically encoded or organic indicators in acute brain slices, related to Figures 3, 4, 5, and 6

(A) Experimental design for the post hoc identification of NSCs used for Ca^{2+} imaging in acute brain slices. (B) Examples of post hoc identification of NSCs. See also examples in Figures 3E, 3F, 3H, 3I, 4C, 5A, 5B, 6A, 6B, 6G, 6H, S2C, and S2D. (C) Experimental design used for labeling NSCs and measuring Ca^{2+} activity in qNSCs and aNSCs using the Rhod2-AM organic Ca^{2+} indicator. The BrdU label-retaining protocol was used in GFAP-GFP mice. One h before preparing the acute brain slices, the Rhod2-AM organic Ca^{2+} indicator was injected into the LV. After imaging, the sections were fixed and immunolabeled for GFP, BrdU, and Ki67. (D) Quantification of the frequency and amplitude of Ca^{2+} events using the Rhod2-AM organic Ca^{2+} indicator.

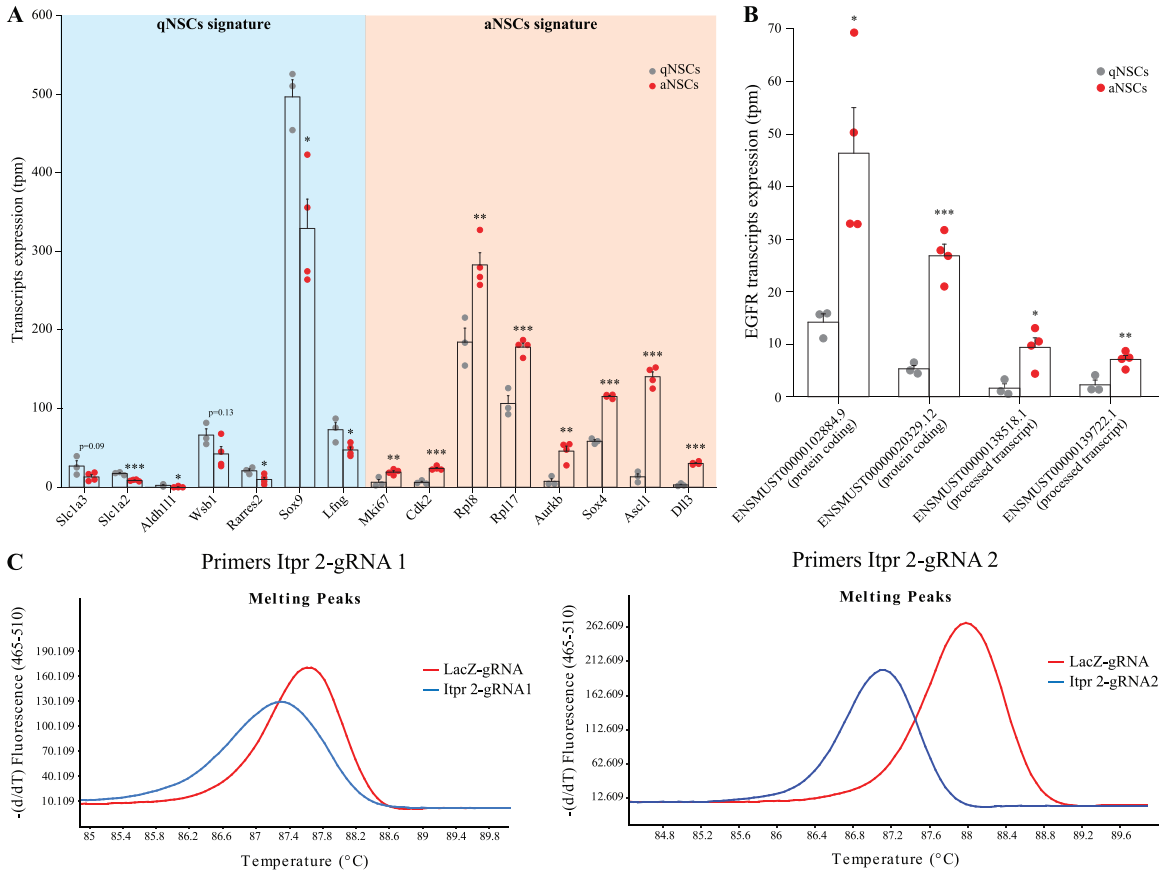

Figure S4. RNA-seq analysis of sorted aNSCs and qNSCs and validation of gRNA efficiency, related to Figures 5 and 6

(A) RNA-seq analysis showing the signature of sorted qNSCs and aNSCs based on the expression of specific genes. To demonstrate the correctness of sorting, we selected genes highly expressed in qNSC and aNSC according to the single cell analysis performed by Llorens-Bobadilla and colleagues (Llorens-Bobadilla et al., 2015). (B) RNA-seq analysis for EGFR transcripts in qNSCs and aNSCs. Note that EGFR transcripts are detected in qNSCs, albeit at lower level than in aNSCs. Data are expressed as means ± SEM 3 and 4 replicates were used for qNSCs and aNSCs, respectively. Statistical significance was determined using a Student's t test. (C) Validation of gRNA efficiency for *Itpr2* by high-resolution melting (HRM) PCR. SVZ cells were isolated and were cultured *in vitro*. The cells were transfected with plasmids carrying Cas9 and various gRNAs. The PCR reaction was performed on genomic DNA, and HRM curves were generated over a 65-95°C range in 0.2°C increments.

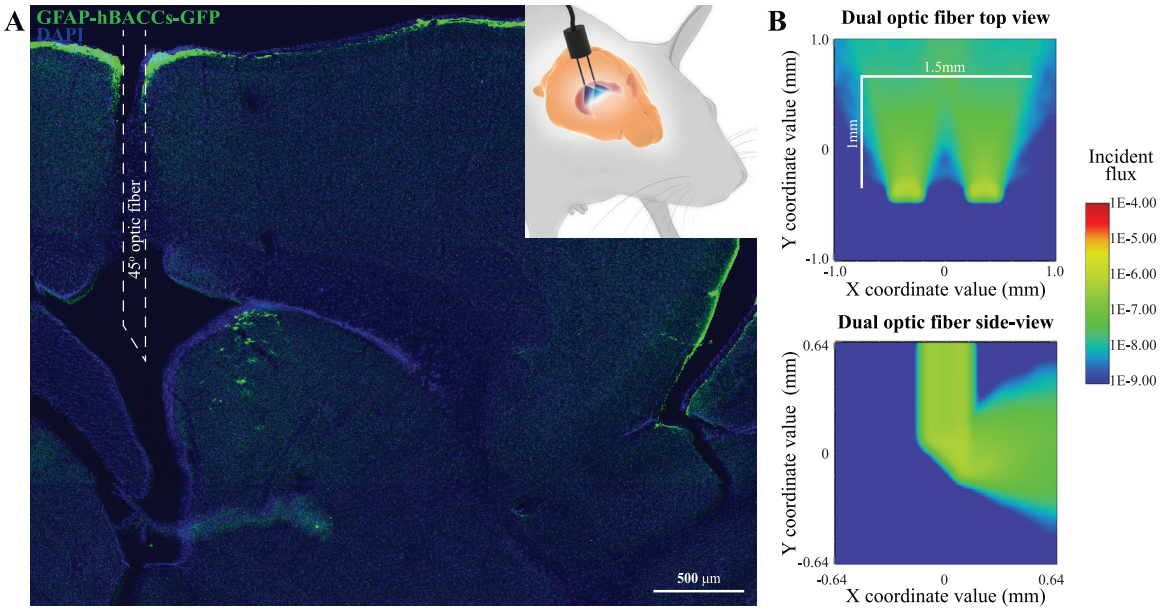

Figure S5. Placement of dual-optic fibers in the lateral ventricle (LV) used for the *in vivo* optogenetic stimulation, related to Figure 7 and STAR methods

(A) Sagittal brain section showing the placement of the optic fiber in the LV. The brain sections were counterstained with DAPI. The placement of the optic fiber is indicated by dashed white rectangles. Note, the placement of only one optic fiber is shown. Inset depicts a schematic diagram showing the placement of dual optic fiber implant in the LV. (B) Top-view (upper panel) and side-view (lower panel) of two optical fibers in the LV at P60-P90 showing the coverage of the medial-lateral portion of the SVZ during optogenetic stimulation. The light diffusion was modeled based on the illumination power, the angle of the fibers, and the pitch (0.7 mm) between two fibers. Note that at least 1.5 mm of medio-lateral SVZ is illuminated. Based on these data, NSCs activation was assessed in the entire medio-lateral portion of the SVZ.